Simulation of 3D elasto-acoustic wave propagation based on a Discontinuous Galerkin Spectral Element method*

Paola F. Antonietti[†1], Francesco Bonaldi[‡1,2], and Ilario Mazzieri[§1]

[1]MOX, Dipartimento di Matematica, Politecnico di Milano, Piazza Leonardo da Vinci 32, 20133 Milano, Italy
[2]Université Côte d'Azur, CNRS, Inria team COFFEE, LJAD, France

Abstract

In this paper we present a numerical discretization of the coupled elasto-acoustic wave propagation problem based on a Discontinuous Galerkin Spectral Element (DGSE) approach in a three-dimensional setting. The unknowns of the coupled problem are the displacement field and the velocity potential, in the elastic and the acoustic domains, respectively, thereby resulting in a symmetric formulation. After stating the main theoretical results, we assess the performance of the method by convergence tests carried out on both matching and non-matching grids, and we simulate realistic scenarios where elasto-acoustic coupling occurs. In particular, we consider the case of Scholte waves, the scattering of elastic waves by an underground acoustic cavity, and a problem of marine seismic exploration. Numerical simulations are carried out by means of the code `SPEED`, available at `http://speed.mox.polimi.it`.

MSC2010: 65M12, 65M60, 86A17

Keywords: Discontinuous Galerkin methods, wave propagation, elasto-acoustics, Spectral Elements, computational geophysics, seismic waves, underground cavities

Introduction

The main goal of this work is to simulate three-dimensional scenarios of elasto-acoustic coupling via a Discontinuous Galerkin Spectral Element (DGSE) discretization (see, in particular, [1] for a comprehensive introduction of the method in the case of elastodynamics). Coupled elasto-acoustic wave propagation arises in several scientific and engineering contexts. In a geophysical framework, a first example one can think of is given by seismic events occurring near coastal environments; another relevant situation where such a problem plays a major role is the detection of underground cavities [2–4]. Elasto-acoustic coupling occurs in structural acoustics as well, when sensing or actuation devices are immersed in an acoustic fluid [5], and also in medical ultrasonics [6, 7].

*This work has been supported by SIR Research Grant no. RBSI14VTOS funded by MIUR – Italian Ministry of Education, Universities, and Research, and by "National Group of Scientific Computing" (GNCS-INdAM).

[†]paola.antonietti@polimi.it
[‡]Corresponding author, francesco.bonaldi@inria.fr
[§]ilario.mazzieri@polimi.it

Typically, an elasto-acoustic coupling arises in the following framework: a space region made up by two subregions, one occupied by a solid (elastic) medium, the other by a fluid (acoustic) one, with suitable transmission conditions imposed at the interface between the two. The aim of such conditions is to account for the following physical properties: (i) the normal component of the velocity field is continuous at the interface; (ii) a pressure load is exerted by the fluid body on the solid one through the interface. In a geophysics context, when a seismic event occurs near a coastal environment, both *pressure* (P) and *shear* (S) waves are generated. However, only P-waves (i.e., whose direction of propagation is aligned with the displacement of the medium) are able to travel through both solid and fluid media, unlike S-waves (i.e., whose direction of propagation is orthogonal to the displacement of the medium), which can travel only through solids. This explains the reason for considering the first interface condition. On the other hand, the second one accounts for the fact that an acoustic wave propagating in a fluid domain gives rise to an *acoustic pressure* exerted on the solid via the interface.

Numerical simulation of elasto-acoustic coupling scenarios has been the subject of a very broad literature. We give below a brief (and by far non-exhaustive) overview of some of the research works carried out so far in this field. Bathe *et al.* [8] and Bermúdez *et al.* [9] considered a displacement-based formulation in both subdomains. Komatitsch *et al.* [10] introduced a Spectral Element method for modeling wave propagation in media with both fluid (acoustic) and solid (elastic) regions. The employed formulation is *symmetric* (i.e., it is made in terms of displacement in elastic regions and velocity potential in acoustic regions), and matching between domains is implemented based on an interface integral in the framework of an explicit prediction-multicorrection staggered time scheme. Bermúdez *et al.* [11] considered a Finite Element approach to the problem based on a pressure formulation in the acoustic domain. Chaljub *et al.* [12] studied a Spectral Element approach for modeling elastic wave propagation in a solid-fluid sphere by taking into account the local effects of gravity, employing a symmetric formulation, as here. Flemisch *et al.* [5] devised a numerical treatment based on two independent triangulations on the elastic and acoustic domains with Finite Elements. Due to the flexible construction of both grids, the finite element nodes on the elastic and acoustic boundary on the interface may, in general, not coincide, so as to allow as much flexibility as possible; as a result, non-conforming grids appear at the interface of the two subdomains. Käser and Dumbser [13] considered a numerical scheme suited for unstructured 2D and 3D meshes based on a Discontinuous Galerkin approach to simulate seismic wave propagation in heterogeneous media containing fluid-solid interfaces, using a formulation in terms of a first-order hyperbolic system in velocity-stress unknowns. The solution across element interfaces is handled by Riemann solvers or numerical fluxes. De Basabe and Sen [14] investigated the stability of the Spectral Element method and the Interior Penalty Discontinuous Galerkin method, considering the Lax-Wendroff method for time stepping and showing that it allows for a larger time step than the usual leap-frog finite difference method, with higher-order accuracy. Wilcox *et al.* [15] studied a high-order Discontinuous Galerkin scheme for the three-dimensional problem based on a velocity-strain formulation, allowing for the solution of the acoustic and elastic wave equations within the same unified framework, based on a first-order system of hyperbolic equations. Soares [16] considered a stabilized time-domain Boundary Element method to discretize each sub-domain. Bottero *et al.* [17] used a time-domain Spectral Element method for simulations of wave propagation in the framework of ocean acoustics. Terrana *et al.* [18] studied a high-order hybridizable Discontinuous Galerkin Spectral Element method, again based on a first-order hyperbolic velocity-strain formulation of the wave equations written in con-

servative form. Very recently, Appelö and Wang [19] devised an energy-based Discontinuous Galerkin approach, again using a symmetric formulation. Finally, a detailed *hp*-convergence analysis of a Discontinuous Galerkin method on polytopal meshes has been presented and validated in a two-dimensional setting in [20], wherein also a well-posedness result has been obtained by a semigroup-based approach.

More generally, concerning the capability of handling nonmatching grids, Bielak *et al.* [21] presented an octree-based Finite Element approach for simulating large-scale earthquake ground motion in realistic basins, combining the low memory per node and good cache performance of finite difference methods with the spatial adaptivity to local seismic wavelengths characteristic of unstructured finite element methods. Tabarrei and Sukumar *et al.* [22] used the quadtree data structure and conforming polygonal interpolants to develop an *h*-adaptive finite element method. The same authors [23] presented an extended Finite Element method on polygonal and quadtree meshes. Šolín *et al.* [24] developed an automatic adaptivity algorithm for the *hp*-Finite Element method which is based on arbitrary-level hanging nodes and local element projections. Gravenkamp *et al.* [25] applied a combination of the transient Scaled Boundary Finite Element Method (SBFEM) and quadtree-based discretization to model wave propagation problems at high frequencies. The SBFEM requires more degrees of freedom than a corresponding spectral element discretization for smooth problems on regular domains, thus the efficiency of the method is improved by proposing a novel approach to reduce the number of auxiliary variables for transient analyses.

In this paper, the unknowns of the problem are the displacement field in the solid domain and the velocity potential in the fluid domain, i.e., we employ a symmetric formulation. The latter, say φ, is defined in terms of the acoustic velocity field $\mathbf{v}_a$ in such a way that $\mathbf{v}_a = -\boldsymbol{\nabla}\varphi$. Also, the acoustic pressure p_a in the fluid region is given by $p_a = \rho_a \dot{\varphi}$, with $\dot{\varphi}$ the first time derivative of the velocity potential.

In the context of earthquake ground motion simulations, the numerical scheme employed has to satisfy the following requirements: *accuracy*, *geometric flexibility*, and *scalability*. To be *accurate*, the numerical method must keep dissipative and dispersive errors low. *Geometric flexibility* is required since the computational domain usually features complicated geometrical shapes as well as sharp discontinuities of mechanical properties. Finally, real-life seismic scenarios are typically characterized by domains whose dimension, ranging from hundreds to thousands square kilometers, is very large compared with the wavelengths of interest. This typically leads to a discrete problem featuring several millions of unknowns. As a consequence, parallel algorithms must be *scalable* in order to efficiently exploit high performance computers.

To comply with these requirements, we employ a Discontinuous Galerkin Spectral Element (DGSE) approach based on a domain decomposition paradigm, which was introduced in [26]. More precisely, the discontinuities are imposed only at the interfaces between suitable nonconforming macroregions, so that the flexibility of the DG methods is preserved while keeping the accuracy and efficiency of Spectral Element (SE) methods and avoiding the proliferation of degrees of freedom that characterize DG methods. We refer to [27] for a more detailed and comprehensive review of discretization methods for seismic wave propagation problems.

The rest of the paper is organized as follows. In Section 1 we give the formulation of the problem and recall the well-posedness result proven in [20] under suitable hypotheses on source terms and initial values. In Section 2 we introduce the DGSE method and present the

formulation of the semi-discrete problem, also recalling a stability result for its formulation in a suitable energy norm, as well as *hp*-convergence results (with h and p denoting the meshsize and the polynomial approximation degree, respectively) for the error in the same norm; a discussion of the fully discrete formulation of the problem is presented as well. Finally, in Section 3, we present several numerical experiments carried out in a three-dimensional setting, with the two-fold aim of verifying the theoretical results and simulating test cases of physical interest. In particular, we verify the convergence rate of the method in Section 3.1 for different kind of meshes. In Section 3.2 we consider the case of Scholte waves. In Section 3.3, we simulate the scattering of elastic waves by an underground acoustic cavity. Finally, in Section 3.4, we consider a problem of marine seismic exploration similar to what was proposed by Käser and Dumbser in [13].

Throughout the paper, we will use standard notation for Sobolev spaces [28]. The Sobolev spaces of vector-valued functions are denoted by $\mathbf{H}^m(\Omega) \equiv [H^m(\Omega)]^d$ and their norms by $\|\cdot\|_{m,\Omega}$, where $\Omega \subset \mathbb{R}^d$ is an open bounded domain of $\mathbb{R}^d$, $d \in \{2,3\}$. We will use the symbol $(\cdot,\cdot)_\Omega$ and $\|\cdot\|_\Omega$ to denote the standard inner product and norm in the space $H^0(\Omega) \equiv L^2(\Omega)$, respectively. We also use the abridged notation $x \lesssim y$ in place of $x \leqslant Cy$, for $C > 0$ independent of the discretization parameters (polynomial degree and meshsize), but possibly depending on the material properties of the media under consideration.

1 Problem statement

In this section, we recall the formulation of the elasto-acoustic problem in its *symmetric* form, i.e., written in terms of the displacement field $\mathbf{u}$ and the velocity potential φ, defined such that the velocity field in the acoustic domain $\mathbf{v}_a$ is given by $\mathbf{v}_a = -\boldsymbol{\nabla}\varphi$ (see [20]). Let $\Omega \equiv \Omega_e \cup \Omega_a \subset \mathbb{R}^3$ denote an open bounded domain with Lipschitz boundary, given by the union of two open disjoint bounded subdomains Ω_e and Ω_a representing the elastic and acoustic regions in their reference configurations, respectively. We denote by $\Gamma_{\mathrm{I}} \equiv \partial\Omega_e \cap \partial\Omega_a$ the *interface* between the two domains. Thus, given a body force $\mathbf{f}_e$ and a scalar volume acoustic source f_a as well as a final time $T > 0$, the strong formulation of the problem reads

$$\begin{cases} \rho_e \ddot{\mathbf{u}} - \mathbf{div}\,\boldsymbol{\sigma}(\mathbf{u}) = \mathbf{f}_e & \text{in } \Omega_e \times (0,T], \\ \boldsymbol{\sigma}(\mathbf{u})\mathbf{n}_e = -\rho_a \dot{\varphi}\,\mathbf{n}_e & \text{on } \Gamma_{\mathrm{I}} \times (0,T], \\ c^{-2}\ddot{\varphi} - \dfrac{1}{\rho_a}\mathrm{div}\,(\rho_a \boldsymbol{\nabla}\varphi) = f_a & \text{in } \Omega_a \times (0,T], \\ \partial\varphi/\partial\mathbf{n}_a = -\dot{\mathbf{u}}\cdot\mathbf{n}_a & \text{on } \Gamma_{\mathrm{I}} \times (0,T], \end{cases} \tag{1}$$

coupled with suitable boundary and initial conditions that are detailed below.

Here, $\rho_e \in L^\infty(\Omega_e)$, $\rho_e > 0$, is the mass density of the elastic region Ω_e; $\boldsymbol{\sigma}(\mathbf{u}) = \mathbb{C}\boldsymbol{\varepsilon}(\mathbf{u}) = \lambda(\mathrm{tr}\,\boldsymbol{\varepsilon}(\mathbf{u}))\mathbf{I} + 2\mu\boldsymbol{\varepsilon}(\mathbf{u})$ is the Cauchy stress tensor; $\mathbb{C}$ is the uniformly elliptic and symmetric fourth-order elasticity tensor, representing a linearly elastic isotropic behavior, with μ and λ the Lamé parameters; $\boldsymbol{\varepsilon}(\mathbf{u}) = \mathrm{sym}\,(\boldsymbol{\nabla}\mathbf{u}) = \frac{1}{2}\left(\boldsymbol{\nabla}\mathbf{u} + \boldsymbol{\nabla}\mathbf{u}^T\right)$ is the strain tensor. Also, we denote by $\rho_a \in L^\infty(\Omega_a)$, $\rho_a > 0$, the density of the acoustic region Ω_a and by $c > 0$ the speed of the acoustic wave.

The transmission conditions on $\Gamma_{\rm I}$ take account of the pressure, of magnitude $\rho_a|\dot\varphi|$, exterted by the acoustic region onto the elastic one through the interface, and of the continuity of the normal component of the velocity field at the interface.

Concerning boundary conditions we assume the following decomposition: $\partial\Omega = (\partial\Omega_e \cup \partial\Omega_a)\backslash\Gamma_{\rm I}$ where $\partial\Omega_e = \Gamma_{e,D} \cup \Gamma_{e,N} \cup \Gamma_{e,NR} \cup \Gamma_{\rm I}$ and $\partial\Omega_a = \Gamma_{a,D} \cup \Gamma_{a,N} \cup \Gamma_{a,NR} \cup \Gamma_{\rm I}$. We denote by $\mathbf{n}_e$ and $\mathbf{n}_a$ the outer unit normal vectors to $\partial\Omega_e$ and $\partial\Omega_a$, respectively. Homogeneous Dirichlet boundary conditions are assigned on $\Gamma_{e,D} \cup \Gamma_{a,D}$, i.e., $\mathbf{u} = \mathbf{0}$ and $\varphi = 0$. Neumann boundary conditions on $\Gamma_{e,N} \cup \Gamma_{a,N}$ are prescribed in term of a surface traction $\mathbf{g}_e$ and a surface acoustic flux g_a as

$$\begin{cases} \boldsymbol{\sigma}(\mathbf{u})\mathbf{n}_e = \mathbf{g}_e & \text{on } \Gamma_{e,N} \times (0,T], \\ \partial\varphi/\partial\mathbf{n}_a = g_a & \text{on } \Gamma_{a,N} \times (0,T]. \end{cases}$$

Non-reflecting boundary conditions are imposed on $\Gamma_{e,NR} \cup \Gamma_{a,NR}$; here, the surface loads are themselves expressed in terms of the time derivatives of the unknowns. In particular, we set

$$\begin{cases} \boldsymbol{\sigma}(\mathbf{u})\mathbf{n}_e = \mathbf{g}_e^\star & \text{on } \Gamma_{e,NR} \times (0,T], \\ \partial\varphi/\partial\mathbf{n}_a = g_a^\star & \text{on } \Gamma_{a,NR} \times (0,T], \end{cases} \tag{2}$$

with $\mathbf{g}_e^\star \equiv \rho_e(c_P - c_S)(\dot{\mathbf{u}} \cdot \mathbf{n}_e)\mathbf{n}_e + \rho_e c_S \dot{\mathbf{u}}$ and $g_a^\star \equiv c^{-1}\dot\varphi$ (see e.g. [5, 29, 30]), where c_P and c_S are the propagation velocities of P (pressure) and S (shear) waves, respectively, given by $c_P = \sqrt{(\lambda + 2\mu)/\rho_e}$ and $c_S = \sqrt{\mu/\rho_e}$. This is commonly referred to in literature as first order absorbing boundary condition [31].

Finally, as initial conditions we set $\mathbf{u}(\cdot,0) = \mathbf{u}_0$ and $\dot{\mathbf{u}}(\cdot,0) = \mathbf{u}_1$ in Ω_e while $\varphi(\cdot,0) = \varphi_0$ and $\dot\varphi(\cdot,0) = \varphi_1$ in Ω_a, for some regular enough functions $\mathbf{u}_0, \mathbf{u}_1, \varphi_0$, and φ_1.

The well-posedness of the problem (1) in suitable functional spaces was proven in [20] under suitable regularity assumptions on the data, in the case $\Gamma_{e,N} \cup \Gamma_{a,N} = \varnothing = \Gamma_{e,NR} \cup \Gamma_{a,NR}$.

2 Numerical discretization

In this section we present the numerical approximation of the weak formulation of (1) through a DGSE method coupled with an explicit *Newmark predictor-corrector staggered* time marching scheme (see [10]). We first introduce the semi-discrete counterpart of (1), observing that the solution of (1) satisfies the following weak form: for any $t \in (0,T]$, and all $(\mathbf{v},\psi) \in \mathbf{H}^1_{\Gamma_{e,D}}(\Omega_e) \times H^1_{\Gamma_{a,D}}(\Omega_a)$,

$$\begin{aligned} (\rho_e\ddot{\mathbf{u}}(t),\mathbf{v})_{\Omega_e} + (c^{-2}\rho_a\ddot\varphi(t),\psi)_{\Omega_a} + \mathcal{A}_e(\mathbf{u}(t),\mathbf{v}) + \mathcal{A}_a(\varphi(t),\psi) + \mathcal{I}_e(\dot\varphi(t),\mathbf{v}) + \mathcal{I}_a(\dot{\mathbf{u}}(t),\psi) \\ = (\mathbf{f}_e(t),\mathbf{v})_{\Omega_e} + (\mathbf{g}_e(t),\mathbf{v})_{\Gamma_{e,N}} + (\mathbf{g}_e^\star(t),\mathbf{v})_{\Gamma_{e,NR}} \\ + (\rho_a f_a(t),\psi)_{\Omega_a} + (\rho_a g_a(t),\psi)_{\Gamma_{a,N}} + (\rho_a g_a^\star(t),\psi)_{\Gamma_{a,NR}}, \end{aligned} \tag{3}$$

where

$$\begin{aligned} \mathcal{A}_e(\mathbf{u},\mathbf{v}) &= (\mathbb{C}\boldsymbol{\varepsilon}(\mathbf{u}),\boldsymbol{\varepsilon}(\mathbf{v}))_{\Omega_e}, & \mathcal{I}_e(\psi,\mathbf{v}) &= (\rho_a\psi\mathbf{n}_e,\mathbf{v})_{\Gamma_{\rm I}}, \\ \mathcal{A}_a(\varphi,\psi) &= (\rho_a\boldsymbol{\nabla}\varphi,\boldsymbol{\nabla}\psi)_{\Omega_a}, & \mathcal{I}_a(\mathbf{v},\psi) &= (\rho_a\mathbf{v}\cdot\mathbf{n}_a,\psi)_{\Gamma_{\rm I}}. \end{aligned} \tag{4}$$

We observe that the second evolution equation has been multiplied by ρ_a to ensure (skew)symmetry of the two interface terms (since $\mathbf{n}_a = -\mathbf{n}_e$).

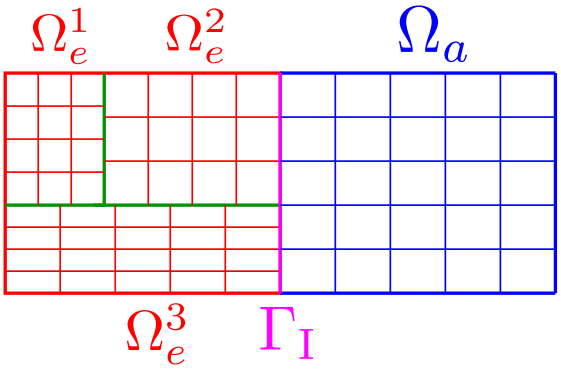

Figure 1: Example of decompositions for the domains Ω_e and Ω_a. Interfaces between elastic regions Ω_e^1, Ω_e^2, and Ω_e^3, characterized by different material properties, are highlighted in green, and the elasto-acoustic interface Γ_{I} is highlighted in purple.

2.1 Partitions and trace operators

We now consider a decomposition $\mathcal{T}_{\Omega_e}$ of Ω_e into L_e nonoverlapping polyhedral regions Ω_e^ℓ, $\ell \in \{1, \dots, L_e\}$, such that $\Omega_e = \bigcup_{\ell=1}^{L_e} \Omega_e^\ell$, with $\Omega_e^\ell \cap \Omega_e^{\ell'} = \varnothing$ for any $\ell \neq \ell'$. This first macropartition is introduced to distinguish elastic materials with different properties (density ρ_e and material moduli λ, μ). On each Ω_e^ℓ, we build a conforming computational mesh $\mathcal{T}_{h_\ell}^e$ of meshsize $h_\ell > 0$ made of disjoint elements $\mathcal{K}_{e,\ell}$, and suppose that each $\mathcal{K}_{e,\ell} \subset \Omega_e^\ell$ is the image through an invertible bilinear map $F_{e,\ell} : \widehat{\mathcal{K}} \to \mathcal{K}_{e,\ell}$ of the unit reference hexahedron $\widehat{\mathcal{K}} = (-1,1)^d$, $d \in \{2,3\}$. Given two adjacent regions $\Omega_e^{\ell^\pm}$, we define an internal face F as the non-empty interior of $\partial\overline{\mathcal{K}_{e,\ell^+}} \cap \partial\overline{\mathcal{K}_{e,\ell^-}}$, for $\mathcal{K}_{e,\ell^\pm} \in \mathcal{T}_{h_{\ell^\pm}}^e$, $\mathcal{K}_{e,\ell^\pm} \subset \Omega_e^{\ell^\pm}$, and collect all the internal faces in the set $\mathcal{F}_{h,e}^i$. Moreover, we define $\mathcal{F}_{h,e}^D$, $\mathcal{F}_{h,e}^N$, and $\mathcal{F}_{h,e}^{NR}$ as the sets of all boundary faces where displacement, tractions, or non-reflecting elastic boundary conditions are imposed, respectively. We collect all the boundary faces *not* laying on Γ_{I} in the set $\mathcal{F}_{h,e}^b$.

Remark 2.1 (Partition of Ω_e). The macro-domains-based partition for the elastic region may also be prescribed by the geometry of the problem, and not necessarily by the variation of material properties. This assumption is made for the sake of simplicity to describe the method.

On the other hand, concerning the acoustic domain Ω_a, since we do not take into account multi-phase fluids, we introduce a conforming grid $\mathcal{T}_h^a$ of Ω_a made by disjoint hexahedral elements $\mathcal{K}_a$. As in the elastic case, we suppose that each $\mathcal{K}_{e,\ell} \subset \Omega_e^\ell$ is the image through an invertible bilinear map $F_a : \widehat{\mathcal{K}} \to \mathcal{K}_a$ of the unit reference hexahedron $\widehat{\mathcal{K}} = (-1,1)^d$, $d \in \{2,3\}$. Also, we define $\mathcal{F}_{h,a}^D$, $\mathcal{F}_{h,a}^N$, and $\mathcal{F}_{h,a}^{NR}$ as the sets of all boundary faces where velocity potential, fluxes, or non-reflecting acoustic boundary conditions are imposed, respectively. We collect all the boundary faces *not* laying on Γ_{I} in the set $\mathcal{F}_{h,a}^b$.

Finally, we collect all faces laying on Γ_{I} in the set $\mathcal{F}_{h,\Gamma_{\mathrm{I}}}$; in this case, $F \in \mathcal{F}_{h,\Gamma_{\mathrm{I}}}$ is the non-empty interior of $\partial\overline{\mathcal{K}_{e,\ell}} \cap \partial\overline{\mathcal{K}_a}$, for given $\mathcal{K}_{e,\ell} \subset \Omega_e^\ell \in \mathcal{T}_{\Omega_e}$ and $\mathcal{K}_a \in \mathcal{T}_h^a$. Implicit in these definitions is the assumption that each face laying on $\partial\Omega_e \cup \partial\Omega_a$ can belong to exactly one of the sets $\mathcal{F}_{h,e}^D$, $\mathcal{F}_{h,e}^N$, $\mathcal{F}_{h,a}^D$, $\mathcal{F}_{h,a}^N$, and $\mathcal{F}_{h,\Gamma_{\mathrm{I}}}$.

Remark 2.2 (Non-matching grids at the elasto-acoustic interface). Notice that the above-detailed framework allows to handle the situation of non-matching grids at the interface Γ_{I}

between the elastic and the acoustic domains (cf. Figure 1). Meshes can therefore be generated independently on each of the domains.

We now introduce the following average and jump operators [32, 33] for mesh faces in the elastic domain. For sufficiently smooth scalar, vector, and tensor fields ψ, $\mathbf{v}$, and $\boldsymbol{\tau}$, we define averages and jumps on an internal face $F \in \mathcal{F}^i_{h,e}$, $F \subset \partial\mathcal{K}_{e,\ell^+} \cap \partial\mathcal{K}_{e,\ell^-}$, with $\mathcal{K}_{e,\ell^\pm} \in \mathcal{T}^e_{h_{\ell^\pm}}$, as follows:

$$
\begin{aligned}
[\![\psi]\!] &= \psi^+\mathbf{n}^+ + \psi^-\mathbf{n}^-, & \{\!\{\psi\}\!\} &= \frac{\psi^+ + \psi^-}{2},\\
[\![\mathbf{v}]\!] &= \mathbf{v}^+ \otimes \mathbf{n}^+ + \mathbf{v}^- \otimes \mathbf{n}^-, & \{\!\{\mathbf{v}\}\!\} &= \frac{\mathbf{v}^+ + \mathbf{v}^-}{2},\\
[\![\boldsymbol{\tau}]\!] &= \boldsymbol{\tau}^+\mathbf{n}^+ + \boldsymbol{\tau}^-\mathbf{n}^-, & \{\!\{\boldsymbol{\tau}\}\!\} &= \frac{\boldsymbol{\tau}^+ + \boldsymbol{\tau}^-}{2},
\end{aligned}
$$

where $\mathbf{a} \otimes \mathbf{b}$ denotes the tensor product of $\mathbf{a}, \mathbf{b} \in \mathbb{R}^3$; $\psi^\pm$, $\mathbf{v}^\pm$ and $\boldsymbol{\tau}^\pm$ are the traces of ψ, $\mathbf{v}$ and $\boldsymbol{\tau}$ on F taken from the interior of $\mathcal{K}_{e,\ell^\pm}$, and $\mathbf{n}^\pm$ is the outer unit normal vector to $\partial\mathcal{K}_{e,\ell^\pm}$. When considering a boundary face $F \in \mathcal{F}^b_{h,e}$, we set $[\![\psi]\!] = \psi\mathbf{n}$, $[\![\mathbf{v}]\!] = \mathbf{v} \otimes \mathbf{n}$, $[\![\boldsymbol{\tau}]\!] = \boldsymbol{\tau}\mathbf{n}$, and $\{\!\{\psi\}\!\} = \psi$, $\{\!\{\mathbf{v}\}\!\} = \mathbf{v}$, $\{\!\{\boldsymbol{\tau}\}\!\} = \boldsymbol{\tau}$. We also use the shorthand notation

$$
\langle \Phi, \Psi \rangle_{\mathcal{F}} = \sum_{F \in \mathcal{F}} (\Phi, \Psi)_F, \qquad \|\Phi\|_{\mathcal{F}} = \langle \Phi, \Phi \rangle_{\mathcal{F}}^{1/2},
$$

for scalar, vector or tensor fields Φ and Ψ and for a given generic collection $\mathcal{F}$ of mesh faces.

2.2 Discontinuous Galerkin Spectral Element approximation

First, concerning the elastic domain Ω_e, we associate with each subdomain Ω_e^ℓ a nonnegative integer $N_{e,\ell} \geqslant 1$, and introduce the finite-dimensional space

$$
\mathbf{V}(\Omega_e^\ell) = \{\mathbf{v} \in \mathbf{C}^0(\overline{\Omega}_e^\ell) : \mathbf{v}_{|\mathcal{K}_{e,\ell}} \circ F_{e,\ell} \in [\mathbb{Q}^{N_{e,\ell}}(\widehat{\mathcal{K}})]^d \ \forall \mathcal{K}_{e,\ell} \in \mathcal{T}^e_{h_\ell}\}, \tag{5}
$$

where $\mathbb{Q}^{N_{e,\ell}}(\widehat{\mathcal{K}})$ is the space of polynomials of degree $N_{e,\ell}$ in each coordinate direction on the unit reference hexahedron $\widehat{\mathcal{K}}$. We then introduce the space $\mathbf{V}(\Omega_e) = \times_{\ell=1}^{L_e} \mathbf{V}(\Omega_e^\ell)$. Concerning the acoustic domain Ω_a we choose a spectral degree $N_a \geqslant 1$ and define the following space:

$$
V(\Omega_a) = \{\psi \in C^0(\overline{\Omega}_a) : \psi_{|\mathcal{K}_a} \circ F_a \in \mathbb{Q}^{N_a}(\widehat{\mathcal{K}}) \ \forall \mathcal{K}_a \in \mathcal{T}^a_h\}. \tag{6}
$$

The semi-discrete DGSE approximation of (3) reads then: $(\mathbf{u}_h, \varphi_h) \in C^2([0,T];\mathbf{V}(\Omega_e)) \times C^2([0,T];V(\Omega_a))$ such that, for all $(\mathbf{v}_h, \psi_h) \in \mathbf{V}(\Omega_e) \times V(\Omega_a)$,

$$
\begin{aligned}
(\rho_e \ddot{\mathbf{u}}_h(t), \mathbf{v}_h)_{\Omega_e} + (c^{-2}\rho_a \ddot{\varphi}_h(t), \psi_h)_{\Omega_a} + \mathcal{A}^e_h(\mathbf{u}_h(t), \mathbf{v}_h) + \mathcal{A}^a_h(\varphi_h(t), \psi_h)\\
+ \mathcal{I}^e_h(\dot{\varphi}_h(t), \mathbf{v}_h) + \mathcal{I}^a_h(\dot{\mathbf{u}}_h(t), \psi_h) = \mathcal{L}^e_h(\mathbf{v}_h) + \mathcal{L}^a_h(\psi_h),
\end{aligned} \tag{7}
$$

with initial conditions $(\mathbf{u}_h(0), \dot{\mathbf{u}}_h(0)) = (\mathbf{u}_{0,h}, \mathbf{u}_{1,h}) \in \mathbf{V}(\Omega_e) \times \mathbf{V}(\Omega_e)$, and $(\varphi_h(0), \dot{\varphi}_h(0)) = (\varphi_{0,h}, \varphi_{1,h}) \in V(\Omega_a) \times V(\Omega_a)$, where $\mathbf{u}_{0,h}, \mathbf{u}_{1,h}, \varphi_{0,h}$, and $\varphi_{1,h}$ are suitable approximations of

the initial data. In (7)

$$
\begin{aligned}
\mathcal{A}_h^e(\mathbf{u},\mathbf{v}) &= \sum_{\Omega_e^\ell\in\mathcal{T}_{\Omega_e}} (\boldsymbol{\sigma}_h(\mathbf{u}),\boldsymbol{\varepsilon}_h(\mathbf{v}))_{\Omega_e^\ell} - \langle\{\!\{\boldsymbol{\sigma}_h(\mathbf{u})\}\!\},[\![\mathbf{v}]\!]\rangle_{\mathcal{F}_{h,e}^i} \\
&\quad - \langle[\![\mathbf{u}]\!],\{\!\{\boldsymbol{\sigma}_h(\mathbf{v})\}\!\}\rangle_{\mathcal{F}_{h,e}^i} + \langle\eta[\![\mathbf{u}]\!],[\![\mathbf{v}]\!]\rangle_{\mathcal{F}_{h,e}^i} && \forall \mathbf{u},\mathbf{v}\in\mathbf{V}(\Omega_e),\\
\mathcal{A}_h^a(\varphi,\psi) &= \sum_{\mathcal{K}_a\in\mathcal{T}_h^a} (\rho_a\boldsymbol{\nabla}\varphi,\boldsymbol{\nabla}\psi)_{\mathcal{K}_a} && \forall \varphi,\psi\in V(\Omega_a),\\
\mathcal{I}_h^e(\psi,\mathbf{v}) &= \langle\rho_a\psi\mathbf{n}_e,\mathbf{v}\rangle_{\mathcal{F}_{h,\Gamma_{\rm I}}} && \forall (\psi,\mathbf{v})\in V(\Omega_a)\times\mathbf{V}(\Omega_e),\\
\mathcal{I}_h^a(\mathbf{v},\psi) &= \langle\rho_a\mathbf{v}\cdot\mathbf{n}_a,\psi\rangle_{\mathcal{F}_{h,\Gamma_{\rm I}}} \equiv -\mathcal{I}_h^e(\psi,\mathbf{v}) && \forall (\mathbf{v},\psi)\in\mathbf{V}(\Omega_e)\times V(\Omega_a),\\
\mathcal{L}_h^e(\mathbf{v}) &= \sum_{\Omega_e^\ell\in\mathcal{T}_{\Omega_e}} (\mathbf{f}_e(t),\mathbf{v})_{\Omega_e^\ell} + \langle\mathbf{g}_e(t),\mathbf{v}\rangle_{\mathcal{F}_{h,e}^N} + \langle\mathbf{g}_e^\star(t),\mathbf{v}\rangle_{\mathcal{F}_{h,e}^{NR}} && \forall \mathbf{v}\in\mathbf{V}(\Omega_e),\\
\mathcal{L}_h^a(\psi) &= \sum_{\mathcal{K}_a\in\mathcal{T}_h^a} (\rho_a f_a(t),\psi)_{\mathcal{K}_a} + \langle\rho_a g_a(t),\psi\rangle_{\mathcal{F}_{h,a}^N} + \langle\rho_a g_a^\star(t),\psi\rangle_{\mathcal{F}_{h,a}^{NR}} && \forall \psi\in V(\Omega_a).
\end{aligned}
\tag{8}
$$

We point out that the fourth identity in (8) holds since $\mathbf{n}_a = -\mathbf{n}_e$ on $\Gamma_{\rm I}$. Here we have set, for any $\mathbf{v}\in\mathbf{V}(\Omega_e)$,

$$
\boldsymbol{\varepsilon}_h(\mathbf{v}) = \frac{1}{2}\left(\boldsymbol{\nabla}_h\mathbf{v} + \boldsymbol{\nabla}_h\mathbf{v}^T\right), \quad \boldsymbol{\sigma}_h(\mathbf{v}) = \mathbb{C}\boldsymbol{\varepsilon}_h(\mathbf{v}),
$$

with $\boldsymbol{\nabla}_h$ the usual broken gradient operator. The discontinuity penalization function $\eta\colon \mathcal{F}_{h,e}^i \to \mathbb{R}$ is defined as follows:

$$
\eta_{|F} = \alpha\{(\lambda+2\mu)^\pm\}_{\rm H}\left\{\left(\frac{N_{e,\ell}^2}{h_\ell}\right)^\pm\right\}_{\rm H}, \quad F\in\mathcal{F}_{h,e}^i,\ F\subset\partial\mathcal{K}_{e,\ell^+}\cap\partial\mathcal{K}_{e,\ell^-}, \tag{9}
$$

with $\mathcal{K}_{e,\ell^\pm}\in\mathcal{T}_{h_{\ell^\pm}}^e$. Here, $\alpha>0$ is a positive constant to be properly chosen, and $\{v^\pm\}_{\rm H} = 2v^+v^-/(v^+ + v^-)$ is the harmonic mean of traces v^+ and v^- of a given scalar field v.

Upon introducing the following norms

$$
\begin{aligned}
\|\mathbf{v}\|_{{\rm DG},e}^2 &= \|\mathbb{C}^{1/2}\boldsymbol{\varepsilon}_h(\mathbf{v})\|_{\Omega_e}^2 + \|\eta^{1/2}[\![\mathbf{v}]\!]\|_{\mathcal{F}_{h,e}^i}^2 && \forall \mathbf{v}\in\mathbf{V}(\Omega_e),\\
\|\mathbf{v}(t)\|_{\mathcal{E}_e}^2 &= \|\rho_e^{1/2}\dot{\mathbf{v}}(t)\|_{\Omega_e}^2 + \|\mathbf{v}(t)\|_{{\rm DG},e}^2 && \forall \mathbf{v}\in C^1([0,T];\mathbf{V}(\Omega_e)),\\
\|\psi(t)\|_{\mathcal{E}_a}^2 &= \|c^{-1}\rho_a^{1/2}\dot{\psi}(t)\|_{\Omega_a}^2 + \|\rho_a^{1/2}\boldsymbol{\nabla}\psi(t)\|_{\Omega_a}^2 && \forall \psi\in C^1([0,T];V(\Omega_a)),
\end{aligned}
\tag{10}
$$

it is possible to prove that bilinear forms $\mathcal{A}_h^e$ and $\mathcal{A}_h^a$ are continuous and coercive. Consequently, a stability result and an error estimate in the above-defined energy norm for the semi-discrete solution can be inferred. We recall those results below; for the sake of readibility, we give a simplified statement of the error estimate (see [20] for a more general framework, and [34] for the purely elastic case).

Theorem 2.3 (Stability of the semi-discrete formulation)**.** *Let* $(\mathbf{u}_h, \varphi_h)$ *be the solution of* (7)*. For a sufficiently large penalty parameter* α *in* (9)*, the following bound holds:*

$$\|\mathbf{u}_h(t)\|_{\mathcal{E}_e} + \|\varphi_h(t)\|_{\mathcal{E}_a} \lesssim \|\mathbf{u}_h(0)\|_{\mathcal{E}_e} + \|\varphi_h(0)\|_{\mathcal{E}_a} + \int_0^t \left(\|\mathbf{f}_e(\tau)\|_{\Omega_e} + \|f_a(\tau)\|_{\Omega_a}\right) \mathrm{d}\tau, \quad t \in (0, T]. \tag{11}$$

Remark 2.4 (Stability parameter). The hidden constant in (11) depends on the stability parameter α in (9) as it is stated in [20, Lemma A.2]. In practice, using $\alpha = \mathcal{O}(10)$ leads to a stable and well-posed problem, see also [34].

Theorem 2.5 (*A priori* error estimate in the energy norm)**.** *Assume that the exact solution of problem* (1) *is such that* $\mathbf{u} \in C^2([0,T]; \mathbf{H}^m(\Omega_e))$ *and* $\varphi \in C^2([0,T]; H^n(\Omega_a))$*, for given integers* $m, n \geqslant 2$*. Then, the following error estimate holds:*

$$\begin{aligned}
&\sup_{t\in[0,T]} \left(\|\mathbf{u}_h(t) - \mathbf{u}(t)\|^2_{\mathcal{E}_e} + \|\varphi_h(t) - \varphi(t)\|^2_{\mathcal{E}_a}\right) \\
&\lesssim \sup_{t\in[0,T]} \left(\sum_{\ell=1}^{L_e} \frac{h_\ell^{2\min(m, N_{e,\ell}+1)-2}}{N_{e,\ell}^{2m-3}} \left(\|\dot{\mathbf{u}}\|^2_{m,\Omega_e^\ell} + \|\mathbf{u}\|^2_{m,\Omega_e^\ell}\right) + \sum_{\mathcal{K}\in\mathcal{T}_h^a} \frac{h_\mathcal{K}^{2\min(n, N_a+1)-2}}{N_{a,}^{2n-3}} \left(\|\dot{\varphi}\|^2_{n,\mathcal{K}} + \|\varphi\|^2_{n,\mathcal{K}}\right) \right) \\
&\quad + \int_0^T \left(\sum_{\ell=1}^{L_e} \frac{h_\ell^{2\min(m, N_{e,\ell}+1)-2}}{N_{e,\ell}^{2m-3}} \left(\|\ddot{\mathbf{u}}\|^2_{m,\Omega_e^\ell} + \|\dot{\mathbf{u}}\|^2_{m,\Omega_e^\ell} + \|\mathbf{u}\|^2_{m,\Omega_e^\ell}\right) \right. \\
&\qquad \left. + \sum_{\mathcal{K}\in\mathcal{T}_h^a} \frac{h_\mathcal{K}^{2\min(n, N_a,+1)-2}}{N_a^{2n-3}} \left(\|\ddot{\varphi}\|^2_{n,\mathcal{K}} + \|\dot{\varphi}\|^2_{n,\mathcal{K}} + \|\varphi\|^2_{n,\mathcal{K}}\right) \right) \mathrm{d}\tau.
\end{aligned}$$

Remark 2.6 (Error in the energy norm). If both meshsizes are quasi-uniform, i.e. $h_\ell \simeq h_e \ \forall \ell \in \{1, \dots, L_e\}$ and $h_\mathcal{K} \simeq h_a \ \forall \mathcal{K} \in \mathcal{T}_h^a$, if the polynomial degree is uniform over elastic regions Ω_e^ℓ, i.e. $N_{e,\ell} = N_e \ \forall \ell \in \{1, \dots, L_e\}$, and if $m \geqslant N_e + 1$ and $n \geqslant N_a + 1$, the following error estimate holds:

$$\sup_{t\in[0,T]} \left(\|\mathbf{u}_h(t) - \mathbf{u}(t)\|_{\mathcal{E}_e} + \|\varphi_h(t) - \varphi(t)\|_{\mathcal{E}_a}\right) \lesssim \ C_\mathbf{u}(T) \frac{h_e^{N_e}}{N_e^{m-3/2}} + C_\varphi(T) \frac{h_a^{N_a}}{N_a^{n-3/2}}, \tag{12}$$

where $C_\mathbf{u}(T)$ and $C_\varphi(T)$ are positive numbers depending on the final time T and the exact solution, along with its time derivatives.

2.3 Fully discrete formulation

Upon fixing polynomial bases for discrete spaces $\mathbf{V}(\Omega_e)$ and $V(\Omega_a)$, see e.g. [20], the semi-discrete algebraic formulation of problem (7) reads

$$\begin{cases} \mathsf{M}_e \ddot{\mathsf{u}}(t) + \mathsf{S}_e \dot{\mathsf{u}}(t) + \mathsf{K}_e \mathsf{u}(t) + \mathsf{C}_e \dot{\boldsymbol{\phi}}(t) = \mathsf{f}_e(t), & t \in (0, T], \\ \mathsf{M}_a \ddot{\boldsymbol{\phi}}(t) + \mathsf{S}_a \dot{\boldsymbol{\phi}}(t) + \mathsf{K}_a \boldsymbol{\phi}(t) + \mathsf{C}_a \dot{\mathsf{u}}(t) = \mathsf{f}_a(t), & t \in (0, T], \end{cases} \tag{13}$$

with initial conditions $\mathsf{u}(0) = \mathsf{u}^0$, $\dot{\mathsf{u}}(0) = \mathsf{v}^0$, $\boldsymbol{\phi}(0) = \boldsymbol{\phi}^0$, and $\dot{\boldsymbol{\phi}}(0) = \boldsymbol{\psi}^0$, and where the vectors $\mathsf{u}(t)$ and $\boldsymbol{\phi}(t)$ represent the expansion coefficients of $\boldsymbol{u}_h(t)$ and $\varphi_h(t)$ in the chosen

bases, respectively. Analogously, M_e, K_e, and C_e are the matrix representations of the bilinear forms $(\rho_e \mathbf{u}, \mathbf{v})_{\Omega_e}$, $\mathcal{A}_h(\mathbf{u}, \mathbf{v})$ and $\mathcal{I}_h^e(\psi, \mathbf{v})$, respectively (see (8)). When elastic absorbing boundary conditions are included in the model, matrix S_e takes account of the boundary term $(\mathbf{g}_e^\star, \mathbf{v})_{\Gamma_{e,NR}}$; otherwise, it is identically equal to zero. On the other hand, M_a, K_a, and $\mathsf{C}_a \equiv -\mathsf{C}_e^\mathsf{T}$ represent the bilinear forms $(c^{-2}\rho_a \varphi, \psi)_{\Omega_a}$, $\mathcal{A}_h^a(\varphi, \psi)$, and $\mathcal{I}_h^a(\mathbf{v}, \psi)$, respectively. When acoustic absorbing boundary conditions are considered, S_a represents the boundary term $(\rho_a g_a^\star, \psi)_{\Gamma_{a,NR}}$. Finally, $\mathsf{f}_e(t)$ and $\mathsf{f}_a(t)$ are the vector representations of linear functionals $\mathcal{L}_h^e$ and $\mathcal{L}_h^a$, respectively.

For the time integration of system (13), as in [10], we employ an explicit Newmark predictor-corrector staggered method [35]; in this case, the scheme is conditionally stable and second-order accurate. We thus subdivide the time interval $[0, T]$ into N_T subintervals of amplitude $\Delta t = T/N_T$ and denote by $\mathsf{u}^n \approx \mathsf{u}(t_n)$, $\mathsf{v}^n \approx \dot{\mathsf{u}}(t_n)$, $\mathsf{a}_e^n \approx \ddot{\mathsf{u}}(t_n)$, $\phi^n \approx \phi(t_n)$, $\psi^n \approx \dot{\Phi}(t_n)$, and $\mathsf{a}_a^n \approx \ddot{\Phi}(t_n)$ the approximations of u, $\dot{\mathsf{u}}$, $\ddot{\mathsf{u}}$, ϕ, $\dot{\phi}$, and $\ddot{\Phi}$ at time $t_n = n\Delta t$, $n \in \{0, \dots, N_T\}$, respectively. Then, along the lines of [10], we exploit the fact that mass matrices are diagonal, and implement an iterative scheme based on a staggered prediction/correction technique. At each time step, we first compute predictors of the solution in both domains:

$$\begin{aligned} \tilde{\mathsf{u}}^{n+1} &= \mathsf{u}^n + \Delta t \mathsf{v}^n + \frac{\Delta t^2}{2}\mathsf{a}_e^n, & \tilde{\mathsf{v}}^{n+1} &= \mathsf{v}^n + \frac{\Delta t}{2}\mathsf{a}_e^n, \\ \tilde{\phi}^{n+1} &= \phi^n + \Delta t \psi^n + \frac{\Delta t^2}{2}\mathsf{a}_a^n, & \tilde{\psi}^{n+1} &= \psi^n + \frac{\Delta t}{2}\mathsf{a}_a^n. \end{aligned} \tag{14}$$

Then, we update the solution in the elastic domain by solving the first equation of (13) for a_e^{n+1}, where the coupling term is evaluated as $-\mathsf{C}_e\tilde{\psi}^{n+1}$, hence using the predictor computed in the acoustic domain. Next, we compute the solution in the acoustic domain by solving the second equation of (13) for a_a^{n+1}, now using the updated solution in the elastic domain to evaluate the coupling term, which is thus given by $-\mathsf{C}_a\mathsf{v}^{n+1}$, where $\mathsf{v}^{n+1} = \tilde{\mathsf{v}}^{n+1} + \frac{\Delta t}{2}\mathsf{a}_e^{n+1}$. We then iterate this algorithm by returning to the first step, this time using the updated solution. The algorithm is summarized in the following scheme.

Newmark predictor-corrector staggered scheme
Given initial conditions $\mathsf{u}^0, \mathsf{v}^0$ and ϕ^0, ψ^0:

compute a_e^0 and a_a^0: $\begin{cases} \mathsf{M}_e\mathsf{a}_e^0 = \mathsf{f}_e^0 - \mathsf{S}_e\mathsf{v}^0 - \mathsf{K}_e\mathsf{u}^0 - \mathsf{C}_e\psi^0, \\ \mathsf{M}_a\mathsf{a}_a^0 = \mathsf{f}_a^0 - \mathsf{S}_a\psi^0 - \mathsf{K}_a\phi^0 - \mathsf{C}_a\mathsf{v}^0; \end{cases}$

for $n = 0$ **to** $N_T - 1$ **do**
- compute predictors $\tilde{\mathsf{u}}^{n+1}, \tilde{\mathsf{v}}^{n+1}, \tilde{\phi}^{n+1}, \tilde{\psi}^{n+1}$ as in (14);
- compute a_e^{n+1}: $\mathsf{M}_e\mathsf{a}_e^{n+1} = \mathsf{f}_e^{n+1} - \mathsf{S}_e\tilde{\mathsf{v}}^{n+1} - \mathsf{K}_e\tilde{\mathsf{u}}^{n+1} - \mathsf{C}_e\tilde{\psi}^{n+1}$;
- update the solution in Ω_e: $\mathsf{u}^{n+1} = \tilde{\mathsf{u}}^{n+1}$, $\mathsf{v}^{n+1} = \tilde{\mathsf{v}}^{n+1} + \frac{\Delta t}{2}\mathsf{a}_e^{n+1}$;
- compute a_a^{n+1}: $\mathsf{M}_a\mathsf{a}_a^{n+1} = \mathsf{f}_a^{n+1} - \mathsf{S}_a\tilde{\psi}^{n+1} - \mathsf{K}_a\tilde{\phi}^{n+1} - \mathsf{C}_a\mathsf{v}^{n+1}$;
- update the solution in Ω_a: $\phi^{n+1} = \tilde{\phi}^{n+1}$, $\psi^{n+1} = \tilde{\psi}^{n+1} + \frac{\Delta t}{2}\mathsf{a}_a^{n+1}$;

end for

3 Numerical results

3.1 Verification test

In this section we solve problem (1) in the parallelepiped $\Omega = (-1,1) \times (0,1) \times (0,1)$ on both matching and non-matching grids (Figure 2), and verify the convergence results shown in Theorem 2.5. Here $\Omega_e = (-1,0) \times (0,1) \times (0,1)$ and $\Omega_a = (0,1)^3$; the interface is thus given by $\Gamma_{\mathrm{I}} = \{0\} \times [0,1] \times [0,1]$. In all cases we compute the energy norm of the error at time $t = 0.1$, cf. (12). For the time discretization we employed the staggered scheme presented in the previous section. The time step employed is $\Delta t = 10^{-6}$. Finally, we choose $\rho_e = 2.7$, $c_P = 6.20$, $c_S = 3.12$, $\rho_a = 1$, and $c = 1$ (cf. [6, 7]). The analytical expression of the exact solution is

$$\begin{aligned} \mathbf{u}(x,y,z;t) &= \left(\cos\left(\frac{4\pi x}{c_P}\right), \cos\left(\frac{4\pi x}{c_S}\right), \cos\left(\frac{4\pi x}{c_S}\right)\right) \cos(4\pi t), \\ \varphi(x,y,z;t) &= \sin\left(\frac{4\pi x}{c}\right) \sin(4\pi t). \end{aligned} \tag{15}$$

The right-hand sides $\mathbf{f}_e$ and f_a corresponding to this solution are both equal to zero. Grids are sequentially refined starting from an initial mesh with uniform meshsize $h = 0.1$ in the matching case (Figure 2a); on the other hand, in the non-matching case (Figure 2b–2c), the submeshes of Ω_e and Ω_a have, respectively, the two initial respective meshsizes $h_e = 0.1$, $h_a = 0.2$ and $h_e = 0.1$, $h_a = 0.15$. Finally, we also considered unstructured matching hexahedral grids, with initial meshsizes $h_e = h_a = 0.2$ (Figure 2d). Numerical tests carried out in both matching (Figure 3), non-matching (Figure 4), and unstructured matching (Figure 5) cases, show that h- and N-convergence rates match those predicted by (12).

3.2 Scholte waves

Scholte waves are an example of boundary waves, propagating along elasto-acoustic interfaces (cf. Figure 6). Their amplitude decays exponentially away from the interface. As in [15], we consider here two half-spaces. The lower half, $z < 0$, is occupied by an elastic medium, and the upper half, $z > 0$, by an acoustic medium.

The derivation of the analytical expressions for Scholte waves was carried out in [36, Section 5.2] in the case of a displacement-based formulation in both domains. We recall hereinafter the essential steps to obtain such expressions. First, in general, the displacement field in both domains is expressed as the sum of the gradient of a scalar potential $\widetilde{\varphi}_\alpha$, $\alpha \in \{a,e\}$, and the curl of a vector potential $\widetilde{\boldsymbol{\psi}}_\alpha$, $\alpha \in \{a,e\}$. Since shear waves are absent in the acoustic domain, we have $\widetilde{\boldsymbol{\psi}}_a = \mathbf{0}$ in Ω_a; on the other hand, it is assumed that $\widetilde{\boldsymbol{\psi}}_e$ is aligned with the y-axis in Ω_e; also, all the fields do not depend on y. The complex amplitudes of the potentials are given by

$$\begin{aligned} \widetilde{\varphi}_e(x,y,z) = B_2 e^{kb_{2p}z} e^{ikx}, \quad \widetilde{\boldsymbol{\psi}}_e(x,y,z) = B_3 e^{kb_{2s}z} e^{ikx} \mathbf{e}_y, \qquad z < 0, \\ \widetilde{\varphi}_a(x,y,z) = B_1 e^{-kb_{1p}z} e^{ikx}, \qquad z > 0 \end{aligned} \tag{16}$$

so that exponential decay occurs for $|z| \to +\infty$. Here, the wavenumber is $k = \omega / c_{\mathrm{sch}}$, for given frequency ω and Scholte wave speed c_{sch}. The decay rates b_{1p}, b_{2p}, and b_{2s} are determined

by substituting expressions (16) in suitable Helmholtz equations; one obtains the following expressions:

$$b_{1p} = \sqrt{1 - \frac{c_{\text{sch}}^2}{c^2}}, \qquad b_{2p} = \sqrt{1 - \frac{c_{\text{sch}}^2}{c_P^2}}, \qquad b_{2s} = \sqrt{1 - \frac{c_{\text{sch}}^2}{c_S^2}}.$$

The displacements in both domains $\mathbf{u}_e$ and $\mathbf{u}_a$ and are thus obtained as

$$\begin{aligned} \mathbf{u}_e(x,y,z;t) &= \text{Re}((\boldsymbol{\nabla}\widetilde{\varphi}_e + \boldsymbol{\nabla}\times\widetilde{\boldsymbol{\psi}}_e)e^{-i\omega t}), \\ \mathbf{u}_a(x,y,z;t) &= \text{Re}((\boldsymbol{\nabla}\widetilde{\varphi}_a)e^{-i\omega t}). \end{aligned} \tag{17}$$

In our formulation, the elastic displacement is simply $\mathbf{u} \equiv \mathbf{u}_e \equiv (u_1, u_2, u_3)$, and the velocity potential φ is obtained by integrating the system of scalar differential equations $\boldsymbol{\nabla}\varphi = -\partial_t \mathbf{u}_a$. Thus, in the light of (17), one obtains the following expressions. For $z < 0$ (elastic region), we have, as in [15],

$$\begin{aligned} u_1(x,y,z;t) &= \text{Re}((ikB_2 e^{kb_{2p}z} - kb_{2s}B_3 e^{kb_{2s}z})e^{i(kx-\omega t)}), \\ u_2(x,y,z;t) &= 0, \\ u_3(x,y,z;t) &= \text{Re}((kb_{2p}B_2 e^{kb_{2p}z} + ikB_3 e^{kb_{2s}z})e^{i(kx-\omega t)}); \end{aligned} \tag{18}$$

and, for $z > 0$ (acoustic region),

$$\varphi(x,y,z;t) = \text{Re}(i\omega B_1 e^{-kb_{1p}z} e^{i(kx-\omega t)}). \tag{19}$$

Notice that the source terms $\mathbf{f}_e$ and f_a corresponding to such analytical expressions are again both equal to zero. In expressions (18)-(19), complex constants B_1, B_2, and B_3 have to satisfy a suitable eigenvalue problem, say $\boldsymbol{\Lambda}\mathbf{B} = \mathbf{0}$ with $\boldsymbol{\Lambda}$ a suitable 3×3 matrix and $\mathbf{B} \equiv [B_1\ B_2\ B_3]^T$, stemming from the transmission conditions imposed on Γ_{I}, i.e. $\boldsymbol{\sigma}(\mathbf{u})\mathbf{n}_e = -\rho_a\dot{\varphi}\mathbf{n}_e$ and $\partial\varphi/\partial\mathbf{n}_a = -\dot{\mathbf{u}}\cdot\mathbf{n}_a$. The value of the Scholte wave speed c_{sch} is thus given by the condition $\det\boldsymbol{\Lambda} = 0$. One can show that a Scholte wave speed exists for arbitrary combinations of material parameters. We use a uniform mesh consisting of 2400 elements (corresponding to a meshsize $h = h_e = h_a = 0.416$) over the domain $(-1,1)\times(-1,1)\times(-20,20)$, and we impose Dirichlet conditions all over the boundary. In the numerical experiments of this section, we choose $\omega = 1$; also, the time step employed is $\Delta t = 10^{-6}$.

We first choose with $\lambda = \mu = 1$ and $\rho_e = 1$ for the elastic medium, and $c = 1$, $\rho_a = 1$ for the acoustic medium (as in [15]). The ratio of the two compressional wave propagation speeds is then $c_P/c = 1$. Based on these values of the material parameters, we obtain, analogously to [15], $c_{\text{sch}} = 0.7110017230197$, which thus gives $k = 1.4064663525$, and we choose $B_1 = -0.3594499773037i$, $B_2 = -0.8194642725978i$, and $B_3 = 1$ as components of a vector $\mathbf{B}$ in the null space of the matrix $\boldsymbol{\Lambda}$.

Then, in order to explore higher velocity contrasts between elastic and acoustic waves, we select $\lambda = 20$, $\mu = 2.5$ for the elastic medium, keeping $c = 1$ and $\rho_a = 1$ for the acoustic one. This implies that $c_P/c = 5$. This choice of values for the material parameters yields $c_{\text{sch}} = 0.9573511944132$, so that $k = 1.0445487568570$, and we now choose $B_1 = 0.0004785577 + 0.4383339278557i$, $B_2 = 0.0006276539484 + 0.5748982984510i$, and $B_3 = -0.6909081865044 + 0.0007543095055i$.

Region	Meshsize (m)	Degree	$\rho_{e/a}\,(\mathrm{kg/m^3})$	$c_P\,(\mathrm{m/s})$	$c_S\,(\mathrm{m/s})$
Ω_e	$h_e = 20$	$N_e = 4$	2700	3000	1734
Ω_a	$h_a = 5$	$N_a = 6$	1024	300	–

Table 1: Test case 3.3. Material properties.

In both cases, as Figure 7 shows, we obtain an asymptotic exponential convergence rate for the error in both the energy and L^2 norms, as expected.

As a final consideration on the accuracy of the proposed method, we show in Figure 8 the maximum relative misfit with respect to the reference solution for two representative points: $\boldsymbol{x}_a = (0, 0, 0.5) \in \Omega_a$ and $\boldsymbol{x}_e = (0, 0, -0.5) \in \Omega_e$, see [37]. In this example, we consider $N_e = N_a = 4$, $\omega = 10$ and the same parameters c_{sch}, B_1, B_2 and B_3 of the previous test case. As one cas see, for both points the maximum misfit is below 5%. This is in agreement with the results shown in Figure 7.

3.3 Underground acoustic cavity

As a last test case, we simulate a seismic wave in the presence of an underground spherical acoustic cavity. A similar problem has been treated in [1, Section 6.1] with a displacement-based approach and also in [4] in a bidimensional setting. This problem arises in several applications, the most important one, besides non-destructive testing, is given by near-surface seismic studies to detect the presence of cavities in the subsoil, which are originated after underground nuclear explosions, and can give rise to resonance effects when a seismic event occurs [4]. In particular, the geometry we consider is the following: the acoustic domain is given by an open ball $\Omega_a = \{\boldsymbol{x} \in \mathbb{R}^3 : \|\boldsymbol{x}\| < R\}$, of radius $R = 30\,\mathrm{m}$, and the elastic one is $\Omega_e = (-L_x, L_x) \times (-L_y, L_y) \times (-L_z, L_z) \backslash \overline{\Omega}_a$ surrounding the cavity, with $L_x = L_y = 600\,\mathrm{m}$ and $L_z = 300\,\mathrm{m}$ (Figure 9). Non-reflecting boundary conditions are imposed on the external elastic boundaries, except on the top one, where a free-surface condition is assigned. The system is excited by a point Ricker wavelet of the following form:

$$\mathbf{f}_e(\boldsymbol{x}, t) = f(t)\mathbf{e}_z\delta(\boldsymbol{x} - \boldsymbol{x}_0), \quad f(t) = f_0\left(1 - 2\pi^2 f_p^2 (t - t_0)^2\right) e^{-\pi^2 f_p^2 (t-t_0)^2}, \tag{20}$$

with $\mathbf{e}_z = (0, 0, 1)$, $\boldsymbol{x}_0 = (200, 0, 300)\,\mathrm{m}$, $t_0 = 0.25\,\mathrm{s}$, $f_0 = 10^{10}\,\mathrm{N}$, and peak frequency f_p. The set of data and space discretization parameters is summarized in Table 1, where we write c_P for c in the case of an acoustic wave. Since the wavelength inside the cavity is much smaller than outside, we are led to choose a finer meshsize inside the cavity, and thus employ the following values: $h_e = 20\,\mathrm{m}$, $h_a = 5\,\mathrm{m}$. Notice that, as explained in [2], meshing a spherical inclusion inside a box containing hexahedral elements is not a trivial task, given that using non-curved elements of meshes inside and outside the cavity leads to empty and overlapping regions which would cause numerical instabilities. We therefore add a small cubic box, with the same elastic properties as Ω_e, around the spherical cavity, in such a way that non-conforming interfaces are present between mesh elements in the small box and in the big box (and the displacement is discontinuous across such interfaces by construction), whereas all interfaces between the small box and the sphere are conforming, cf. a cross section in Figure 10. We use polynomial degrees $N_e = 4$ and $N_a = 6$ on the elastic and acoustic domains, respectively, and we set the

time-step to $\Delta t = 10^{-5}\,\mathrm{s}$. The latter value is chosen in order to prevent the time integrator, described in Section 2.3, from possible numerical instability. Finally, we remark that for all the cases presented below we choose the penalty paramter α in (9) equal to 10.

We compute the solution wavefield for different values of the peak frequency in the Ricker signal (20): $f_p = 11\,\mathrm{Hz}$, $22\,\mathrm{Hz}$, and $33\,\mathrm{Hz}$. Those values guarantee that the ratio between the diameter of the sphere Ω_a and shortest wavelength of (20) is approximately given by $\mathcal{R} = 2R/\lambda_{min} \approx 0.5, 1$ and 1.5, respectively. Notice that we have considered as a dominant period of (20) the value $T_D = \frac{\sqrt{6}}{\pi f_p}$ and the minimal characteristic wave speed $c_S = 1734\ m/s$.

Figure 10 shows the z-component u_z of the displacement field in the subsoil and the acoustic velocity potential φ in the spherical cavity at times $t = 0.4\,\mathrm{s}$ and $t = 0.5\,\mathrm{s}$ when $\mathcal{R} \approx 1$, whereas Figure 11 shows the same quantities when $\mathcal{R} \approx 0.5$. We remark that, in the first case (Figure 10), the elastic wave detects the acoustic cavity: spherical wavefronts are generated due to refraction phenomena between the cavity and the subsoil, since the wavelength corresponding to the value $f_p = 22\,\mathrm{Hz}$ is comparable with the diameter of the cavity. On the other hand, if the peak frequency is reduced by a factor two (Figure 11), we observe that the interaction of the elastic wave with the cavity is weaker than in the first case, since the corresponding wavelength is twice as much as in the first case. In both cases, since outside the sphere the material is stiff, the acoustic wave remains trapped within the cavity over time and it generates reflection and refraction effects. These phenomena can be better represented and remarked if the time histories of a number of monitored points in the elastic and acoustic domains are considered. In particular, we took into account an X-shaped set of points in a square cross section of the computational domain lying in the xz-plane, centered in the origin, with side $600\,\mathrm{m}$ (Figure 12). Time histories of points in the subsoil and in the underground cavity are showcased in Figure 13 for the three cases $\mathcal{R} \approx 0.5, 1$ and 1.5. In particular, reflection phenomena for elastic waves are clearly more remarkable in the last case than in the first. As expected, point A being the closest one to the location of the seismic source, is the first to undergo a displacement impulse, which is then delayed for the other points; the same occurs in the second case. Finally, in all cases, we clearly see that the acoustic wave remains trapped in cavity over time, due to persistent reflections.

3.4 Discontinuous sinusoidal bathymetry

To further demonstrate the flexibility and potential of the proposed method, we consider the following test problem of marine seismic exploration, similarly to what was proposed in [13]. The computational domain $\Omega = (0, 3200\,\mathrm{m}) \times (0, 3200\,\mathrm{m}) \times (-2000\,\mathrm{m}, 0)$ includes a water layer at rest on top of an elastic solid with the fluid-solid interface modeling a complicated bathymetry that has smooth and discontinuous features. The explicit equation for the $xy-$dependent elevation z of the acoustic-elastic interface is given by

$$z(x,y) = A\sin(k_x x)\sin(k_y y) - \begin{cases} 800\,\mathrm{m} & x > 1600\,\mathrm{m} \text{ and } y > 1600\,\mathrm{m}, \\ 500\,\mathrm{m} & \text{otherwise}, \end{cases} \tag{21}$$

with amplitude $A = 300\,\mathrm{m}$ and wavenumbers $k_x = 8/6400\pi\,\mathrm{m}^{-1}$ and $k_y = 6/6400\pi\,\mathrm{m}^{-1}$. Note that (21) represents a sinusoidal interface with a jump, as shown in Figure 14. The model is discretized by 369.892 Hexahedral elements of an average edge length of $60\,\mathrm{m}$ in

Region	Meshsize (m)	Degree	$\rho_{e/a}\,(\mathrm{kg/m^3})$	$c_P\,(\mathrm{m/s})$	$c_S\,(\mathrm{m/s})$
Ω_e	$h_e = 60$	$N_e = 4$	2500	3400	1963
Ω_a	$h_a = 60$	$N_a = 4$	1020	1500	–

Table 2: Test case 3.4. Material properties.

either the acoustic and elastic domains. The top (acoustic) surface is treated as a free-surface, whereas the remaing (acoustic and elastic) domain boundaries are absorbing boundaries. The material parameters are given in Table 2. A compressional point source of a $f_p = 10\,\mathrm{Hz}$ Ricker wavelet, cf. (20), is used at position $\boldsymbol{x}_s = (1600, 1600, -300)\,\mathrm{m}$. The computation is carried out by choosing a polynomial degree $N_a = N_e = 4$, leading to approximately 60 million of degrees of freedom, by fixing the time step $\Delta t = 10^{-5}\,\mathrm{s}$ and a final time $T = 2\,\mathrm{s}$. The calculation was performed in approximately 16 hours by using 512 cores of the Marconi-A2 cluster located at CINECA, Italy. Snapshots of the computed elastic velocity wavefield in the z direction together with the computed acoustic velocity potential are reported in Figure 15. It is possible to observe the reflected wave at the top surface, the P-to-S converted wave in the solid, headwaves that follow the smoothly varying fluid-solid interface. Furthermore, the sharp corner in the middle of the domain, where a discontinuity in the ocean-bottom appears, acts like a diffractor point, see Figure 15. We point out that the major benefit of this approach is to produce highly accurate synthetic data-sets for geometrically complex models. These results can be used in modern geophysical exploration techniques and 3D seismic data-processing algorithms to reveal, with high precision, geometrically complex subsurface structures.

4 Conclusions and perspectives

We have presented a Discontinuous Galerkin Spectral Element method for the approximation of the elasto-acoustic evolution problem. Several numerical experiments carried out in a three-dimensional framework have been discussed, both to verify the theoretical results and to simulate a scenario of physical interest. Our approach is well-suited to comply with the requirements for the discretization of heterogeneous seismic wave propagation problems (geometric flexibility, high-order accuracy, and flexibility); in addition, it allows for the treatment of non-matching grids at the interface between the elastic and the acoustic domains, which can therefore be generated independently on each of the domains. All numerical experiments have been carried out using the computer code `SPEED` [30], freely available at `http://speed.mox.polimi.it`.

A future work consists in the extension to general polyhedral meshes in `SPEED`, in order to tame the computational cost of mesh generation and enhance the geometrical flexibility of the numerical discretization.

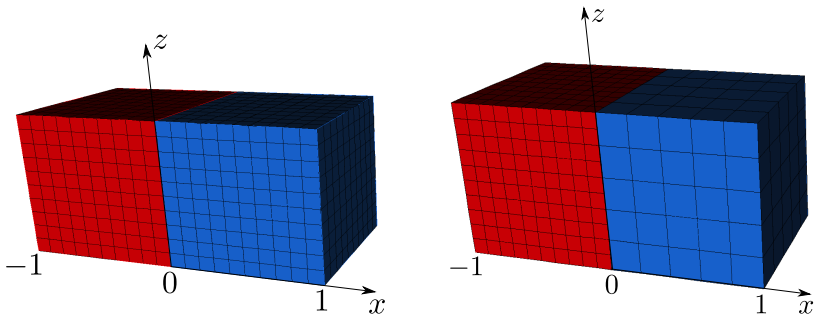

(a) $h = h_e = h_a = 0.1$ (b) $h_e = 0.1$, $h_a = 0.2$

(c) $h_e = 0.1$, $h_a = 0.15$ (d) $h_e = h_a = 0.2$

Figure 2: Test case 3.1. Computational domain with matching (a), non-matching (b)–(c), and unstructured matching (d) hexahedral meshes.

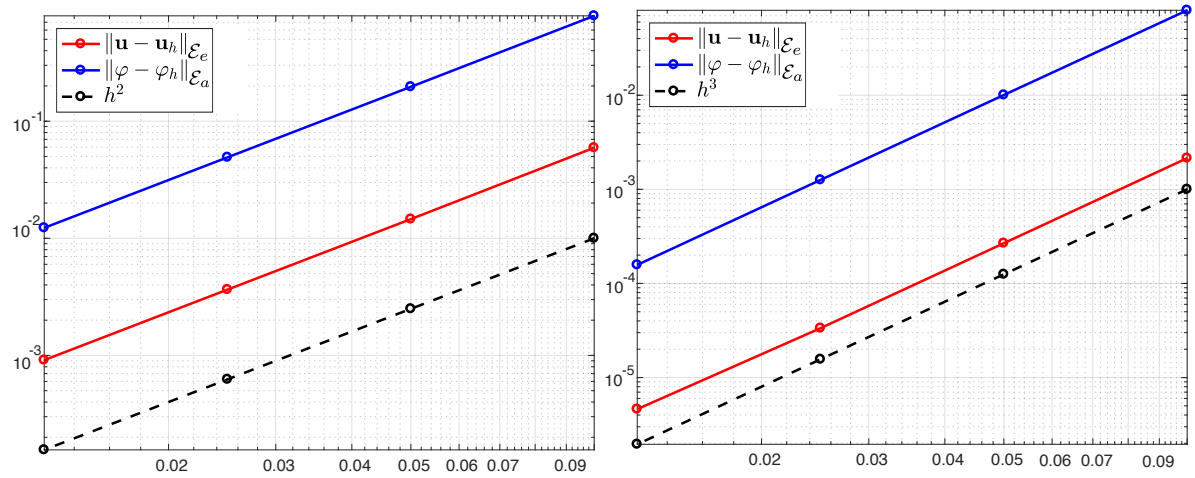

(a) $N = N_e = N_a = 2$

(b) $N = N_e = N_a = 3$

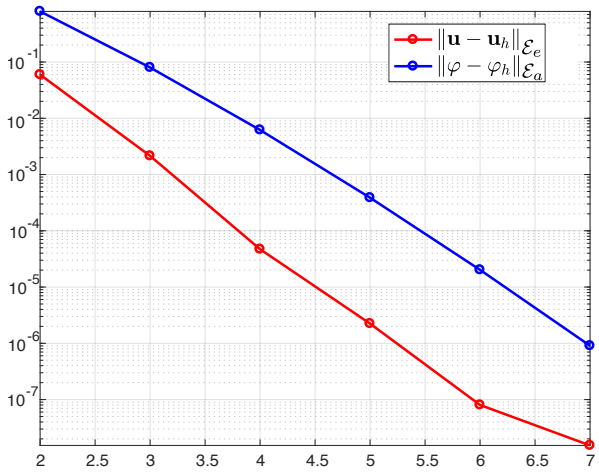

(c) $N = N_e = N_a$ ranging from 2 to 7

Figure 3: Test case 3.1. Error in the energy norm vs. h (a)–(b) and N (c) at $t = 0.1\,\mathrm{s}$.

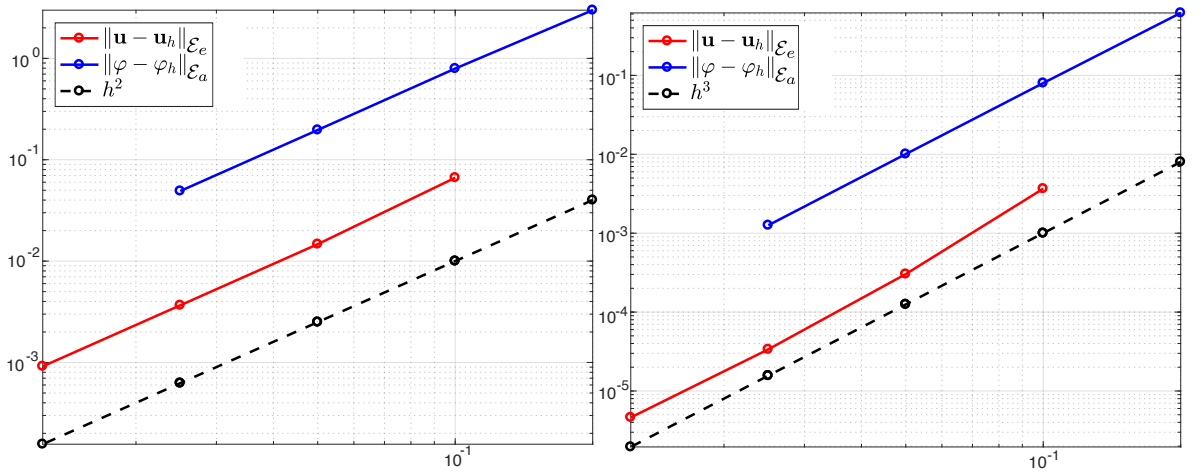

(a) $N = N_e = N_a = 2$ (b) $N = N_e = N_a = 3$

(c) $N = N_e = N_a = 2$ (d) $h_e = 0.1$, $h_a = 0.2$, N ranging from 2 to 7

Figure 4: Test case 3.1. Error vs. h (a)–(b)–(c) and N (d) at $t = 0.1\,\mathrm{s}$ for non-matching hexahedral grids. Initial meshsizes are $h_e = 0.1$, $h_a = 0.2$ in (a) and (b), and $h_e = 0.1$, $h_a = 0.15$ in (c).

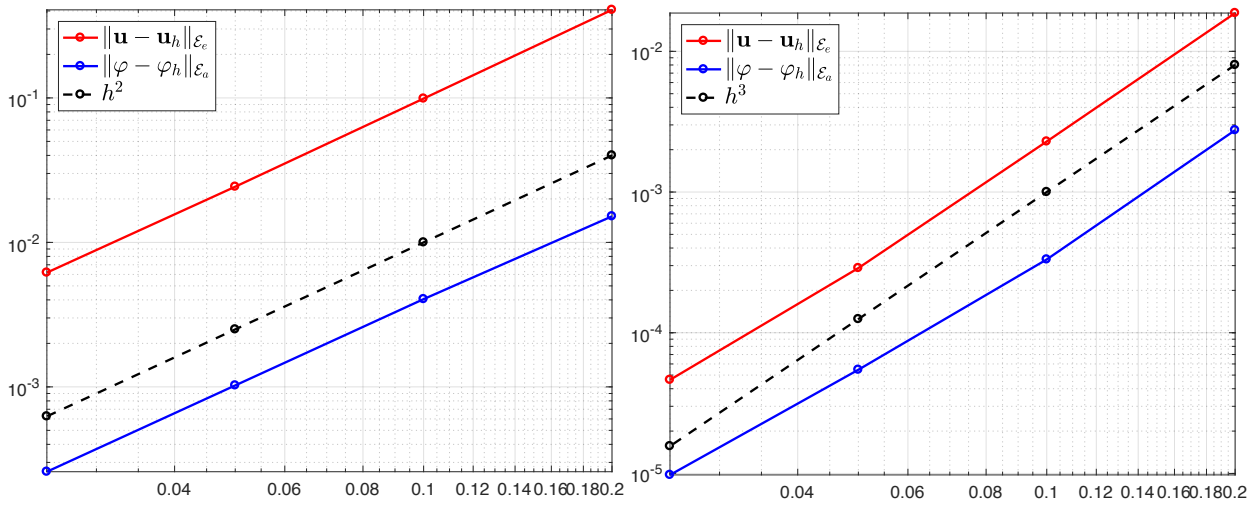

(a) $N = N_e = N_a = 2$ (b) $N = N_e = N_a = 3$

Figure 5: Test case 3.1. Error vs. h at $t = 0.1\,\mathrm{s}$ for unstructured matching hexahedral grids. Initial meshsizes are $h_e = h_a = 0.2$.

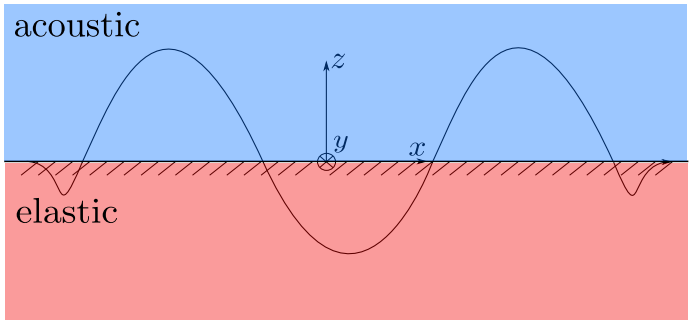

Figure 6: Test case 3.2. Scholte wave at the interface between an elastic medium and an acoustic one.

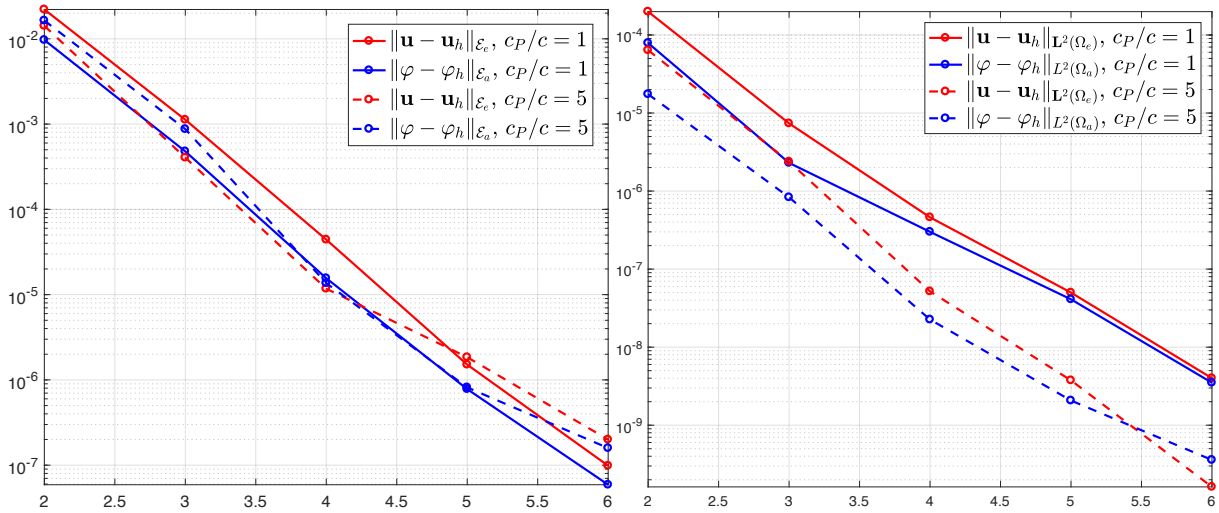

(a) (b)

Figure 7: Test case 3.2. Error in the energy (a) and L^2 (b) norms vs. N at $t = 0.1\,\mathrm{s}$, with N ranging from 2 to 6. Continuous lines correspond to the case of $c_P/c = 1$, dashed lines to the case of $c_P/c = 5$.

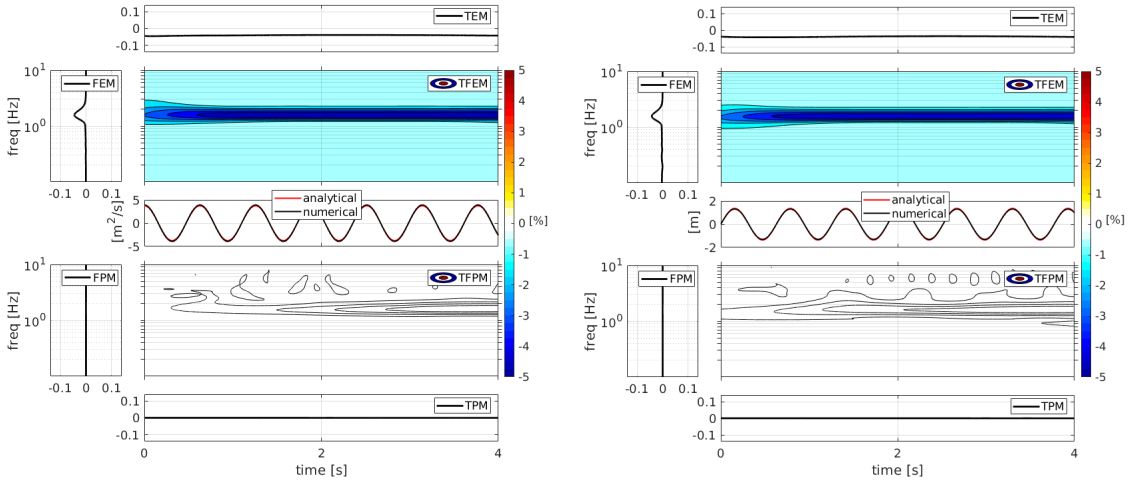

(a) (b)

Figure 8: Test case 3.2. Comparison in time and frequency domain between the analytical solution (red line) and the numerical one (black line). Relative misfit computed with [37] for the acoustic velocity potential in $\boldsymbol{x} = (0, 0, 0.5)$ (a) and for the elastic displacement $\boldsymbol{u}_z$ in $\boldsymbol{x} = (0, 0, -0.5)$ (b). *FEM*: frequency-dependent envelope misfit; *TEM*: time-dependent envelope misfit; *TFEM*: time-frequency envelope misfit; *FPM*: frequency-dependent phase misfit; *TPM*: time-dependent phase misfit; *TFPM*: time-frequency phase misfit.

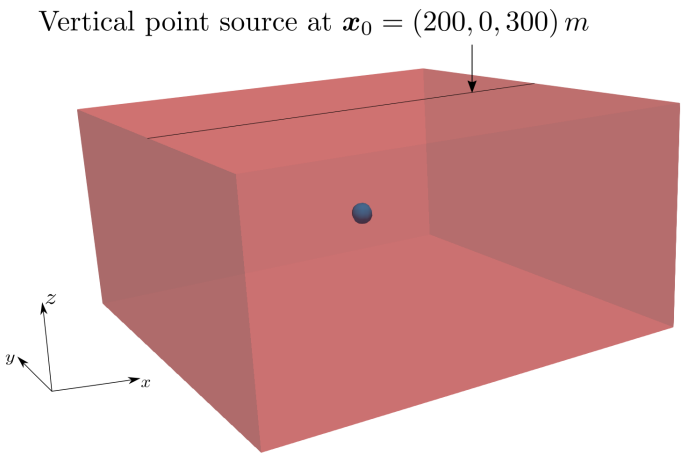

Figure 9: Test case 3.3. Geometry of the computational domain for the case of a seismic wave in the presence of an underground cavity.

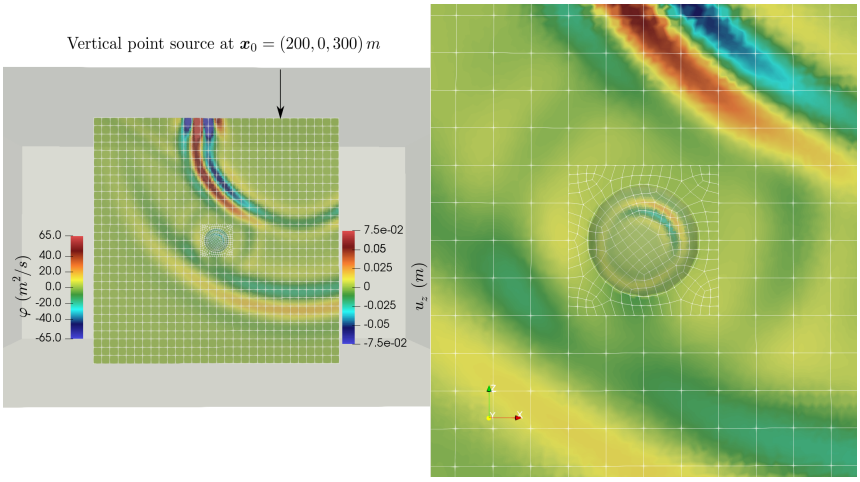

(a)

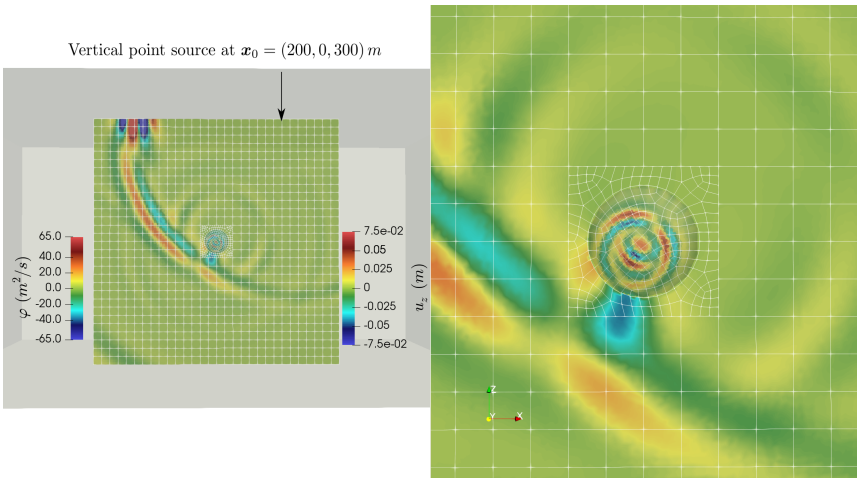

(b)

Figure 10: Test case 3.3. Displacement along the z-direction and velocity potential at time $t = 0.4\,\mathrm{s}$ (a) and $t = 0.5\,\mathrm{s}$ (b) for $\mathcal{R} \approx 1$.

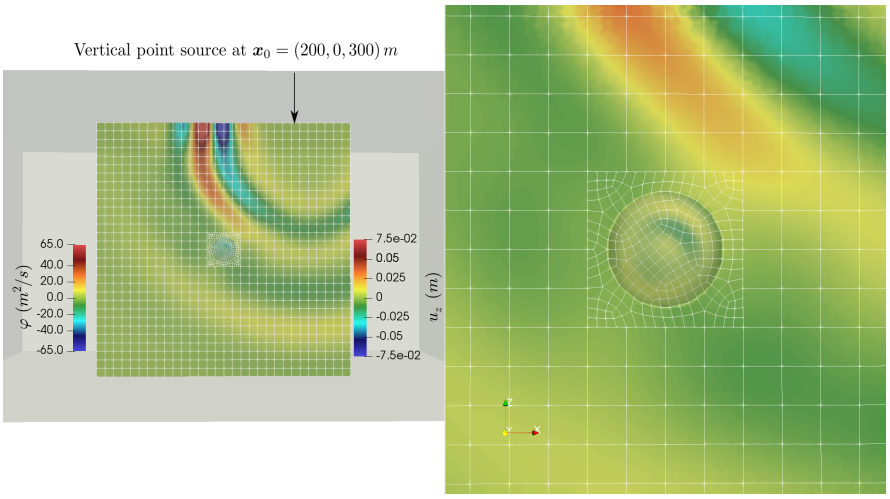

(a)

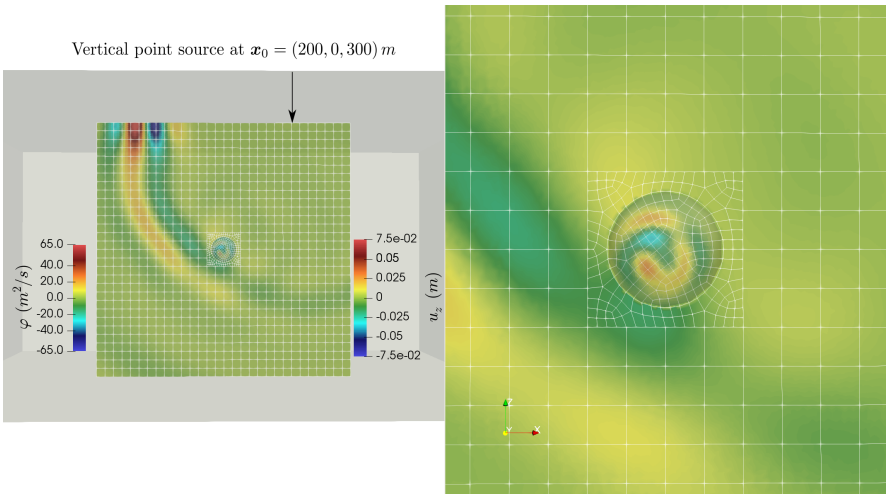

(b)

Figure 11: Test case 3.3. Displacement along the z-direction and velocity potential at time $t = 0.4\,\mathrm{s}$ (a) and $t = 0.5\,\mathrm{s}$ (b) for $\mathcal{R} \approx 0.5$.

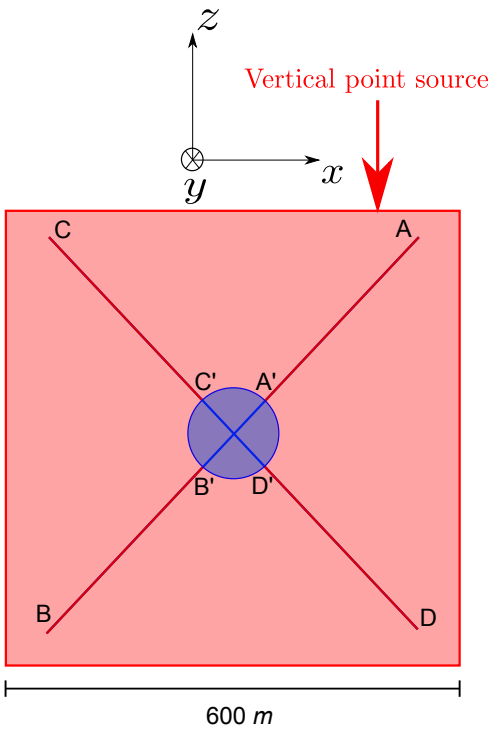

Figure 12: Test case 3.3. Set of monitors in the square cross section of the computational domain lying in the xz-plane, centered in the origin, with side 600 m.

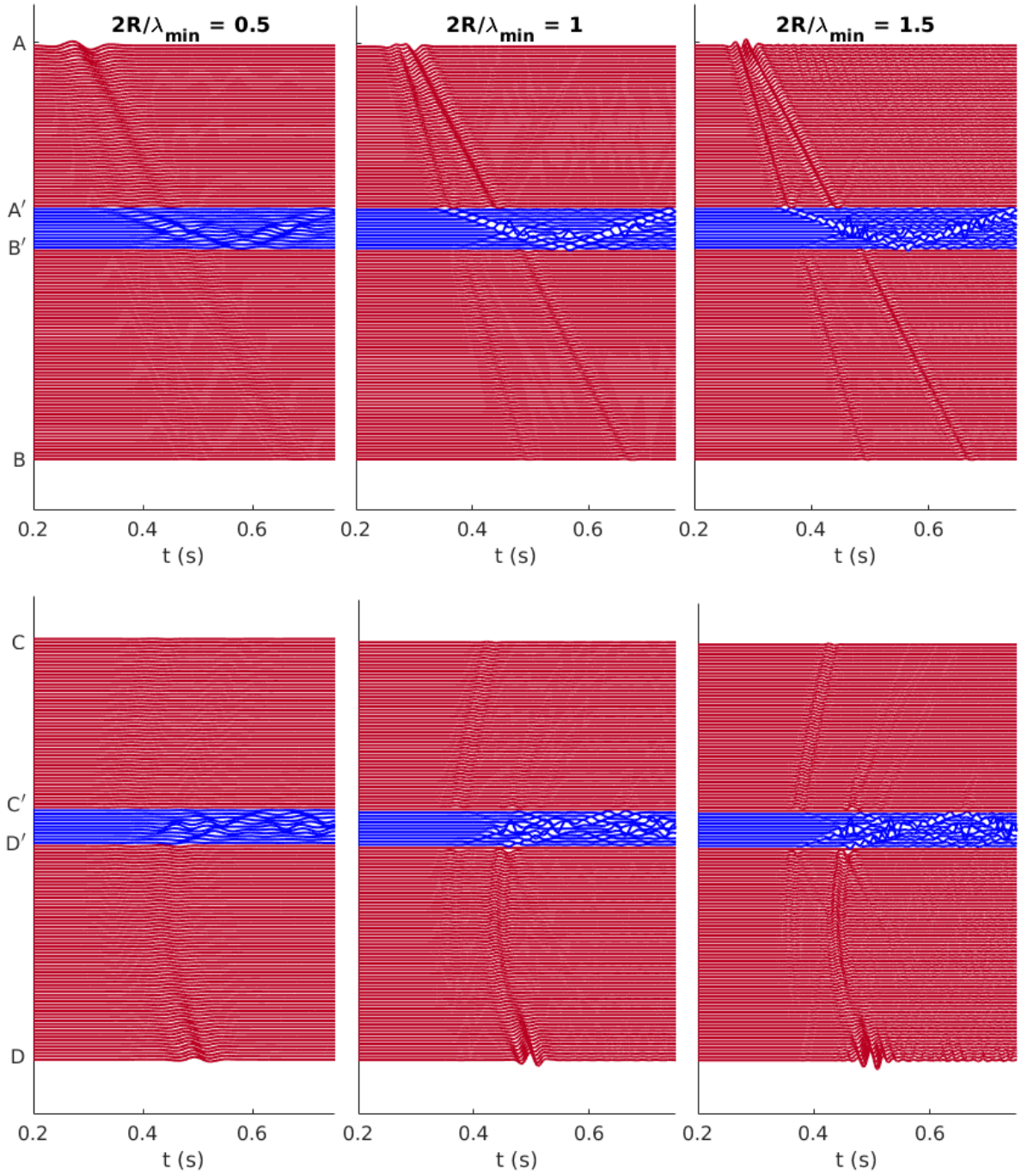

Figure 13: Test case 3.3. Time histories of the computed displacement (resp. velocity potential) wavefield along the z-direction for the monitored points in the elastic subsoil (red) (resp. the acoustic cavity (blue)) for the three cases considered $\mathcal{R} \approx 0.5$ (left), $\mathcal{R} \approx 1$ (center) and $\mathcal{R} \approx 1.5$ (right). For visualization purposes the velocity potential has been multiplied by a factor 0.01.

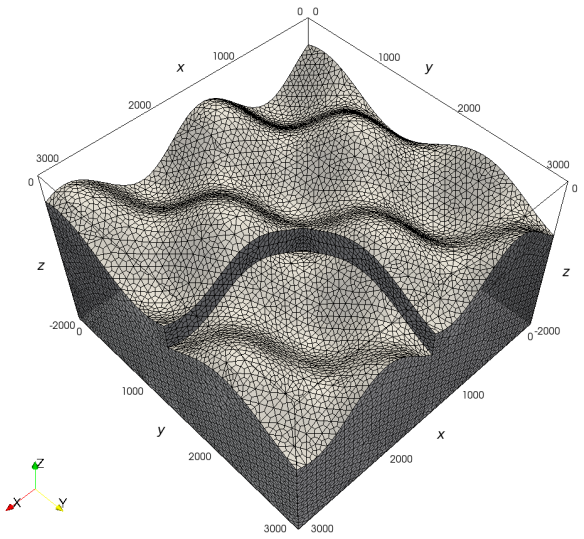

Figure 14: Test case 3.4. Hexahedral discretization of the elastic medium with discontinuous sinusoidal ocean-bottom topography. The conforming discretization of the above acoustic domain is not shown so as to make visible the complicated fluid-solid interface.

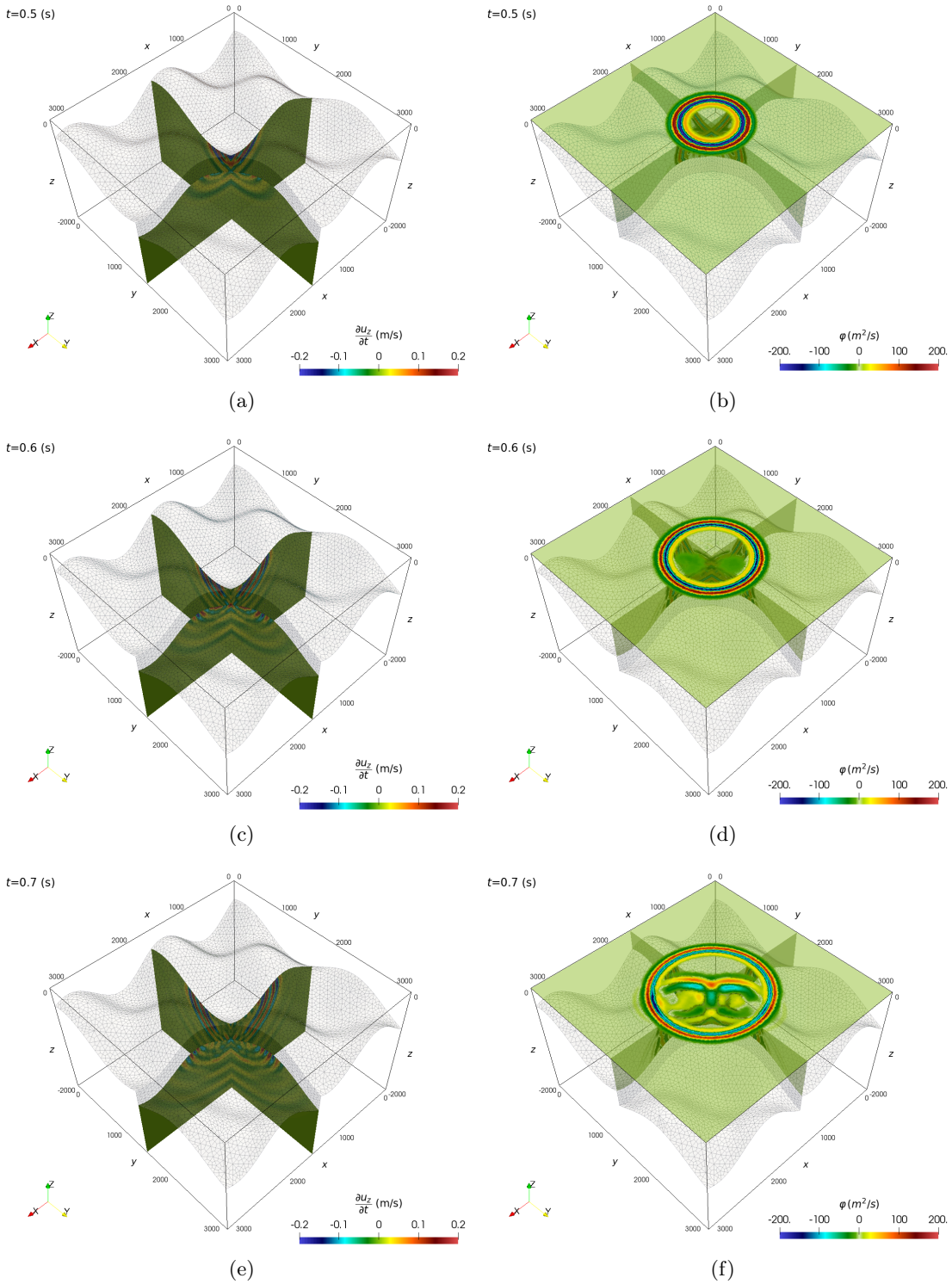

Figure 15: Test case 3.4. Snapshots of the computed elastic velocity wavefield in the z direction together with the computed acoustic velocity potential for time instants (a-b) $t = 0.5\ s$, (c-d) $t = 0.6\ s$ and (e-f) $t = 0.7\ s$.

References

[1] A. Ferroni. "Discontinuous Galerkin spectral element methods for the elastodynamics equation on hybrid hexahedral-tetrahedral grids". PhD thesis. Politecnico di Milano, 2017.

[2] S. Esterhazy, F. Schneider, I. Mazzieri, and G. Bokelmann. *Insights into the modeling of seismic waves for the detection of underground cavities*. Tech. rep. 67/2017. MOX, Politecnico di Milano, 2017.

[3] S. Esterhazy, F. Schneider, I. Perugia, and G. Bokelmann. "Application of high-order finite-element method to the P-wave propagation around and inside an underground cavity". In: *Geophysics* 82 (2017), T197–T206.

[4] F. Schneider, S. Esterhazy, I. Perugia, and G. Bokelmann. "Seismic resonances of spherical acoustic cavities". In: *Geophysical Prospecting* 65 (2017), pp. 1–24.

[5] B. Flemisch, M. Kaltenbacher, and B. I. Wohlmuth. "Elasto–acoustic and acoustic–acoustic coupling on non-matching grids". In: *Int. J. Numer. Meth. Engng* 67 (2006), pp. 1791–1810.

[6] S. Mönköla. "Numerical simulation of fluid-structure interaction between acoustic and elastic waves". PhD thesis. University of Jyväskylä, 2011.

[7] S. Mönköla. "On the accuracy and efficiency of transient spectral element models for seismic wave problems". In: *Adv. Math. Phys.* (2016).

[8] K. J. Bathe, C. Nitikitpaiboon, and X. Wang. "A mixed displacement-based finite element formulation for acoustic fluid-structure interaction". In: *Computers & Structures* 56 (1995), pp. 225–237.

[9] A. Bermúdez, L. Hervella–Nieto, and R. Rodríguez. "Finite element computation of three-dimensional elastoacoustic vibrations". In: *Journal of Sound and Vibration* 219 (1999), pp. 279–306.

[10] D. Komatitsch, C. Barnes, and J. Tromp. "Wave propagation near a fluid-solid interface: a spectral-element approach". In: *Geophysics* 65 (2000), pp. 623–631.

[11] A. Bermúdez, P. Gamallo, L. Hervella–Nieto, and R. Rodríguez. "Finite element analysis of pressure formulation of the elastoacoustic problem". In: *Numer. Math.* 95 (2003), pp. 29–51.

[12] E. Chaljub, Y. Capdeville, and J. P. Vilotte. "Solving elastodynamics in a fluid-solid heterogeneous sphere: a parallel spectral element approximation on non-conforming grids". In: *J. Comput. Phys.* 187 (2003), pp. 457–491.

[13] M. Käser and M. Dumbser. "A highly accurate discontinuous Galerkin method for complex interfaces between solids and moving fluids". In: *Geophysics* 73 (2008), T23–T35.

[14] J. D. De Basabe and M. K. Sen. "Stability of the high-order finite elements for acoustic or elastic wave propagation with high-order time stepping". In: *Geophys. J. Int.* 181 (2010), pp. 577–590.

[15] L. C. Wilcox, G. Stadler, C. Burstedde, and O. Ghattas. "A high-order discontinuous Galerkin method for wave propagation through coupled elastic-acoustic media". In: *J. Comput. Phys.* 229 (2010), pp. 9373–9396.

[16] D. Soares Jr. "Coupled Numerical Methods to Analyze Interacting Acoustic-Dynamic Models by Multidomain Decomposition Techniques". In: *Math. Probl. Eng.* (2011).

[17] A. Bottero, P. Cristini, and D. Komatitsch. "An axisymmetric time-domain spectral-element method for full-wave simulations: Application to ocean acoustics". In: *J. Acoust. Soc. Am.* 140 (2016).

[18] S. Terrana, J. P. Vilotte, and L. Guillot. "A spectral hybridizable discontinuous Galerkin method for elastic–acoustic wave propagation". In: *Geophys. J. Int.* 213 (2018), pp. 574–602.

[19] D. Appelö and S. Wang. "An energy based Discontinuous Galerkin method for coupled elasto-acoustic wave equations in second order form". In: *Int. J. Numer. Meth. Engng* 119 (2019), pp. 618–638.

[20] P. F. Antonietti, F. Bonaldi, and I. Mazzieri. "A high-order discontinuous Galerkin approach to the elasto-acoustic problem". In: *Comput. Methods Appl. Mech. Engrg.* (2019). Published online. DOI: 10.1016/j.cma.2019.112634.

[21] J. Bielak, O. Ghattas, and E.J. Kim. "Parallel Octree-Based Finite Element Method for Large-Scale Earthquake Ground Motion Simulation". In: *CMES – Computer Modeling in Engineering and Sciences* 10 (2005), pp. 99–112.

[22] A. Tabarrei and N. Sukumar. "Adaptive computations on conforming quadtree meshes". In: *Finite Elem. Anal. Des.* 41 (2005), pp. 686–702.

[23] A. Tabarrei and N. Sukumar. "Extended finite element method on polygonal and quadtree meshes". In: *Comput. Methods Appl. Mech. Engrg.* 197 (2008), pp. 425–438.

[24] P. Šolín, J. Červený, and I. Doležel. "Arbitrary-level hanging nodes and automatic adaptivity in the hp-FEM". In: *Math. Comput. Simulation* 77 (2008), pp. 117–132.

[25] H. Gravenkamp, A.A. Saputra, C. Song, and C. Birk. "Efficient wave propagation simulation on quadtree meshes using SBFEM with reduced modal basis". In: *Int. J. Numer. Meth. Engng* 110 (2017).

[26] P. F. Antonietti, I. Mazzieri, A. Quarteroni, and F. Rapetti. "Non-conforming high order approximations of the elastodynamics equation". In: *Comput. Methods Appl. Mech. Engrg.* 209 (2012), pp. 212–238.

[27] P. F. Antonietti, A. Ferroni, I. Mazzieri, R. Paolucci, A. Quarteroni, C. Smerzini, and M. Stupazzini. "Numerical modeling of seismic waves by discontinuous spectral element methods". In: *ESAIM:ProcS* 61 (2018), pp. 1–37.

[28] R. A. Adams and J. J. F. Fournier. *Sobolev Spaces*. Academic Press, 2003.

[29] D. Komatitsch, J. P. Vilotte, R. Vai, Castillo–Covarrubias, and F. J. Sánchez–Sesma. "The Spectral Element method for elastic wave equations–application to 2-D and 3-D seismic problems". In: *Int. J. Numer. Meth. Engng* 45 (1999), pp. 1139–1164.

[30] I. Mazzieri, M. Stupazzini, R. Guidotti, and C. Smerzini. "SPEED: SPectral Elements in Elastodynamics with Discontinuous Galerkin: a non-conforming approach for 3D multi-scale problems". In: *Int. J. Numer. Meth. Engng* 95 (2013), pp. 991–1010.

[31] R. Stacey. "Improved transparent boundary formulations for the elastic-wave equation". In: *Bulletin of the Seismological Society of America* 78 (1988), pp. 2089–2097.

[32] D. N. Arnold, F. Brezzi, B. Cockburn, and L. D. Marini. "Unified analysis of discontinuous Galerkin methods for elliptic problems". In: *SIAM J. Numer. Anal.* 39 (2002), pp. 1749–1779.

[33] D. N. Arnold, F. Brezzi, R. S. Falk, and L. D. Marini. "Locking-free Reissner–Mindlin elements without reduced integration". In: *Comput. Methods Appl. Mech. Engrg.* 196 (2007), pp. 3660–3671.

[34] P. F. Antonietti, B. Ayuso de Dios, I. Mazzieri, and A. Quarteroni. "Stability analysis of discontinuous Galerkin approximations to the elastodynamics problem". In: *J. Sci. Comput.* 68 (2016), pp. 143–170.

[35] T. J. R. Hughes. *The finite element method, linear static and dynamic finite element analysis*. Prentice-Hall International, 1987.

[36] A. A. Kaufman and A. L. Levshin. *Acoustic and Elastic Wave Fields in Geophysics, III*. Vol. 39. Methods in Geochemistry and Geophysics. Elsevier B. V., 2005.

[37] M. Kristeková, J. Kristek, P. Moczo, and S. M. Day. "Misfit Criteria for Quantitative Comparison of Seismograms". In: *Bulletin of the Seismological Society of America* 96 (2006), pp. 1836–1850.